2019-01-01

Compressive and Rheological Deformation Analysis of Large Area Pellet-fed Material Extrusion 3D Printed Parts in Relation to In Situ Thermal Imaging

Eduardo Meraz Trejo
University of Texas at El Paso, emerazt@gmail.com

COMPRESSIVE AND RHEOLOGICAL DEFORMATION ANALYSIS OF LARGE AREA PELLET-FED MATERIAL EXTRUSION 3D PRINTED PARTS IN RELATION TO IN SITU THERMAL IMAGING

EDUARDO MERAZ TREJO

Master's Program in Mechanical Engineering

APPROVED:

David Espalin, Ph.D., Chair

Ryan Wicker, Ph.D.

Amit Lopes, Ph.D.

Charles Ambler, Ph.D.
Dean of the Graduate School

This thesis is dedicated to my family, whose relentless support and encouragement made this journey possible.

COMPRESSIVE AND RHEOLOGICAL DEFORMATION ANALYSIS OF LARGE AREA PELLET-FED MATERIAL EXTRUSION 3D PRINTED PARTS IN RELATION TO IN SITU THERMAL IMAGING

by

EDUARDO MERAZ TREJO, B.S.M.E, B.A.E.

THESIS

Presented to the Faculty of the Graduate School of

The University of Texas at El Paso

in Partial Fulfillment

of the Requirements

for the Degree of

MASTER OF SCIENCE

Department of Mechanical Engineering

THE UNIVERSITY OF TEXAS AT EL PASO

May 2019

Acknowledgements

First and foremost I would like to express my gratitude towards my mentor and advisor, Dr. David Espalin. With his continuous support and guidance, as well as his constructive teaching and suggestions, he led me to complete the work presented in this thesis, and encouraged me to go beyond and above to develop a passion for additive manufacturing. I am also grateful towards my colleagues, Xavier Jimenez and Fernando Rodriguez Lorenzana, learning alongside me, helped me to complete the experimental methodology in the work presented here. Xavier Jimenez and Kazi Billah served as mentors to me, whose experience in technical writing assisted me to complete my graduate thesis work.

I would also like to thank my colleagues who were in Dr. Espalin's research group alongside me, including Jose Motta, Jose Coronel, Christopher Minjares, Leonardo Rodriguez, and Emerson Armendariz, for providing me with constructive feedback and advice during our weekly research meetings. I would also like to thank Mrs. Mireya Perez, the manager of the W.M. Keck Center for 3D Innovation at the University of Texas at El Paso, as well as other members of the staff, for providing my colleagues and myself with the tools and resources to perform research to assist in the growth and development of the 3D manufacturing industry and beyond. I would also like to thank Dr. Ryan Wicker for being the pioneer of the W.M. Keck Center at the university, granting the students and the university a remarkable institution devoted to technological development.

In addition, I would like to thank my family, in particular my grandparents Jose and Eloisa, for being alongside me in this journey, who never stopped inspiring me and supporting me to pursue my education and become a better person. I would also like to thank my parents, sister, aunt and cousin, for being there for me in this journey.

Abstract

In large area pellet extrusion additive manufacturing, the temperature of the substrate just prior to the deposition of a new subsequent layer has an effect on the overall structure of the part. Warping and cracking occur if the substrate temperature is below a specific threshold, but also deformation and deposition adhesion failure occur if the substrate temperature is above a certain threshold just prior to deposition of a new layer. Currently, Big Area Additive Manufacturing (BAAM) machine users mitigate this problem by trial and error, which is costly and may result in decreased mechanical properties, monetary losses and time inefficiencies.

Through thermal imaging, the range of temperatures present during the printing of a 20% by weight carbon fiber reinforced acrylonitrile butadiene styrene (ABS-20CF) single-bead wall via the BAAM machine was identified - specifically the temperature range at which deformation occurs. Compression tests were then performed to understand the compressive behavior vis-à-vis temperature, at a range identified in the thermography experiments. Ten sets of compression tests were performed at temperatures of 90 °C, 110 °C, 130 °C, 150 °C, 170 °C, 190 °C, 200 °C, 210 °C, 230 °C, and 250 °C. Furthermore, to explain the experimental compression behavior, optical imaging was performed to create a relationship between porosity in the printed bead to plateau regions observed in the compression curves at temperatures of 170 °C and below. Finally, rheological testing was performed to evaluate the viscoelastic properties of BAAM-printed ABS-20CF at temperatures of 160 °C, 170 °C, 180 °C, 190 °C, 200 °C, 210°C, 220 °C, and 230 °C – the range of temperatures where deformation was observed during thermal imaging.

It was concluded that the substrate experiences deformation if it is above a temperature of 200 °C at the time a new layer is deposited. Thermal imaging revealed that the range of temperatures at which deformation occurs is between 195 °C and 210 °C. Compression testing

revealed that the compressive strength of the material has an inverse relationship with temperature. However, the compressive behavior remained virtually the same at temperatures of 200 °C and above. Finally, rheological testing revealed that 200 °C is the onset temperature in which the material transitions from the rubbery plateau region into the rubbery flow region, where the viscous properties are more prevalent and the material behavior becomes akin to a liquid. These results suggest that the compressive load that the substrate can withstand prior to deformation is smaller than the load exerted by the extruder depositing a new layer, in conjunction with the load exerted by the tamper mechanism. The low compressive strength at temperatures of 200 °C and higher, is then attributed to a change in viscoelastic properties, where the material is more prone to plastic deformation.

Using the information obtained from experimental testing, two new single-bead wall geometries were printed. The temperature of these two walls were controlled with the aid of the 1-dimensional thermal model developed by Oak Ridge National Laboratories (ORNL). The temperature of the substrate in the first print was controlled to remain at approximately 195 °C. Twenty layers were printed successfully; no deformation due to temperature was observed in the print. In the second print, the substrate temperature was controlled to remain at approximately 220 °C. Deformation was seen during the deposition of layer 6, where layer 5 experienced significant deformation. Every layer after experienced the same deformation, where the substrate deformed in such a way that new layers were deposited diagonally above the substrate instead of directly above it. This lead to new layers being deposited in such "zig-zag" diagonal fashion. The combined deformation was such, that at the time of deposition of layer 11, the layer was extruded into mid-air.

In conclusion, if the substrate temperature was at a temperature greater than 200 °C at the time a new layer was deposited, the material suffered compressive deformation and flow to the side, as if the new layer was deposited diagonally above it. A new layer will be deposited following this initial deformation. Eventually, when a new layer is deposited, the part will be considerably shorter due to the combined deformation, and the new material will be extruded into mid-air. The thermal model developed by ORNL is an effective tool to predicting and controlling the temperature of a single-bead thin wall print.

Table of Contents

List of Tables

List of Figures

Chapter 1

Introduction

1.1 Background

Additive manufacturing (AM) is a fabrication technology that enables the user to build custom parts from the ground up on a layer-by-layer basis. This technology started in the 1980s, and has had a resurgence in recent years, partly due to the newfound interest in new manufacturing materials, particularly polymers and polymer composites, that lead to higher economical and time efficiencies. Among the advantages of additive manufacturing, are the ability to create complex geometries, the high manufacturing precision, lower production costs, and the reduction of material waste when compared with conventional subtractive manufacturing techniques. These and more advantages have made additive manufacturing in recent years to become a big focus of research – with papers published rising from 1000 in 2011 to 16000 in 2012 – as well as high commercial interest, particularly in the aerospace and automotive industries. It is not uncommon to see additive manufacturing to be used with the purpose of rapid prototyping, tooling, or simply creating parts that are used in vehicle frames, airplane simulators, and an airplane's fuselage.

Additive manufacturing is a technology that is not limited to a small range of materials – being able to print metals, ceramics, and many types of polymers for a wide variety of purposes. The basic mechanism of an AM system is as follows:

1) A model is created in a computer aided design software (CAD) or an existing part is reverse engineered
2) The CAD is processed into a Standard Tesselation Language (STL) file, through which subsequent slicing creates a layer-by-layer decomposition

3) The file is processed into a G-Code, which contains movement and temperature instructions for the gantry and heated nozzle systems
4) The part is printed layer by layer from the ground up

The introduction of Big Area Additive Manufacturing (BAAM) to the 3-D printing industry brought a wide range of new advantages to a field already full of innovation. BAAM is a thermoplastic extruding machine that works in a similar fashion to a conventional 3D printing. A CAD model is processed, converted into an STL file, then into a G-Code, which then gives instructions to melt the material and extrude it through a nozzle, whose deposition coordinate locations are controlled by a gantry system, and as can be seen in the diagram in Figure 1, below. The BAAM machine exclusively uses thermoplastics as its feeding material, in the shape of pellets. These pellets are absorbed and fed into a heated single-screw extruder, where the solid pellets become semi-molten and are then deposited through a heated nozzle onto a heated bed, as can be seen in the Figure 2 diagram, below.

1.2 Motivation

While BAAM has a larger print envelope, a faster printing speed, and lower production costs - as compared to conventional desktop material extrusion systems – it still has some considerable design and physical limitations. A particular challenge that BAAM is facing today is the nearly erratic relationship between print quality and temperature distribution and history. Temperature control is important to ensure robust adhesion between layers, dimensional accuracy, and an overall successful print. Particularly, when the temperature of the top layer of a part just prior to the deposition of a subsequent layer is above a certain threshold, the deposited layer will have poor adhesion to the bottom layers, collapse and thereby causing an overall print failure. Therefore, the motivation of this work is to evaluate the relationship between high temperatures

and mechanical properties that lead to the structural failure of a printed part. This manuscript will analyze the failure mechanisms present during the continuous print of a single-bead, thin-wall section vis-à-vis a temperature analysis. The relationship between the compressive stress, compressive strain, rheological properties, and temperature will be evaluated in order to understand and ultimately prevent the failure mechanisms that occur during the printing of a part as a consequence of high temperatures.

1.3 Thesis Objectives

The thesis objectives are listed as follows:

1. Analyze the temperature evolution present in the printing of a carbon fiber reinforced acrylonitrile butadiene styrene part
2. Evaluate the upper temperature threshold present during structural print failure
3. Discover the relationship between temperature and mechanical properties of carbon fiber reinforced acrylonitrile butadiene styrene (ABS), vis-à-vis printing parameters
4. Incorporate a previously developed 1-dimensional heat transfer model into a print
5. Develop a set of printing parameters, vis-à-vis temperature control, to ensure a successful print

1.4 Thesis Outline

This thesis is divided into six chapters. Chapter 1 offers an introduction to the thesis, as well as the motivation and background for this work. Chapter 2 is a literature review, with relevant previous work on which this work is based on and supplemented by. These works summarize the relevant literature on compression testing, a background of Big Area Additive Manufacturing, infrared imaging, the basic principles and concepts behind additive manufacturing, material characterization, as well as thermal and compressive analysis of thermoplastics, among others.

Chapter 3 describes the methodology of this research work in detail, narrating the materials and processes used, as well as explaining the experimental procedures that led to the conclusion of this research. Chapter 4 summarizes the results of the experimental data obtained, and discusses its relevant significance in relation to the objectives of this work. Finally, Chapter 5 contains the conclusion of this paper as well as recommendations for future work.

Chapter 2

Literature Review

2.1 Introduction

The introduction of Big Area Additive Manufacturing (BAAM) to the 3-D printing industry brought a wide range of new advantages to a field already full of innovation. A relatively new technology, coming to the market in 2015, BAAM works conceptually as a conventional additive manufacturing machine. The BAAM printing process starts with a CAD file that is converted into a Standard Tesselation Language (STL) file – which divides the structure of the model into many layers stacked on top of each other [1]. From there, the STL file is converted into a G-Code, i.e. instructions for the AM machine regarding deposition coordinate location, extrusion temperature, standby time between layers, etc. Once the G-Code is uploaded into the machine, the part is ready to be printed. The main difference between BAAM and conventional material extrusion systems, such as fused deposition modeling (FDM) and fused filament fabrication (FFF), besides lower production costs, is that BAAM can print volumes up to 240 inches by 90 inches by 72 inches – 10 times larger than conventional printing – and with feed rates of up to 80 pounds per hour.

However, while BAAM has significant advantages over conventional desktop 3D printing systems, it still has some considerable design and physical limitations [2]. A particular challenge that BAAM is facing today is the nearly erratic relationship between print quality and temperature distribution and history. Temperature control is important to ensure robust adhesion between layers, dimensional accuracy, and an overall successful print [2, 3]. Efforts have been conducted to analyze and select the appropriate range of temperature processing parameters to ensure a successful print. A work by Ajinjeru *et al*. suggested upper and lower temperature bounds for

processing such that the structural integrity of the material is not compromised – higher bound – and at the same time remains above the temperature at which processes such as injection molding and extrusion are performed – lower bound [3]. Although the higher temperature bound suggested by Ajinjeru *et al.* ensure that the part doesn't lose stiffness due to structural degradation, printing at temperatures below their suggested threshold doesn't safeguard the user from a failed print. This particular issue has been noted by several works, including an investigation conducted by Roschli *et al*. [2], where it is mentioned that high temperatures of the top layer just prior to deposition of a subsequent layer are correlated to poor structural rigidity, resulting in poor dimensional accuracy, low inter-layer adhesion, and overall a failed print. Roschli *et al*. conclude that a way of mitigating this failure associated with high temperatures is to manipulate the layer times of printing in order to control the temperature –i.e., by adding a waiting time between layer depositions, the temperature of the top layer decreases. However, no thermal mechanical analysis is performed, and no specific guidelines or temperature thresholds were suggested in order to have a successful print. Currently, BAAM users modify print parameters based on empirical data and user experience. The philosophy of trial and error can lead to economic and time inefficiencies, thus diminishing the advantages that BAAM has over conventional desktop systems.

2.2 Additive Manufacturing (AM)

Although the manufacturing process followed by AM technologies is similar, as previously described, it is the author's opinion that a background on the different additive manufacturing process categories will enrich the content of this document, and provide the reader a better understanding of the main concepts behind additive manufacturing. As such, the seven different additive manufacturing process categories identified by ASTM International will now be described, vis-à-vis the working mechanism and concept behind the technology, the materials

used, and the challenges faced by each category. Illustrations depicting the operating mechanism of every category are depicted on Appendix A. The categories are:

1. Binder-jetting
2. Directed Energy Deposition
3. Material Extrusion
4. Material Jetting
5. Powder Bed Fusion
6. Sheet Lamination
7. Vat Photopolymerization

As far as hardware is concerned, although the components might be different from AM to AM system, they all follow the basic functions. The AM machines have a material input mechanism (e.g. material reservoir, pellet feeder, powder dispenser), a control system mechanism to selectively build a layer into position, and a surface in which the material is placed on. The differences between the AM categories will be described in detail in the following sections.

Most 3D printing technologies follow the same process prior to printing, starting with a CAD file, which the user will have to convert into a format which only captures the surface geometry of a digital model - in most occasions as an STL file. The STL file is then processed through a software that generates instructions containing the information necessary for the two dimensional, layer-by-layer manufacturing process from the ground up: specified coordinates for every layer for the print head to follow (also known as toolpath), the acceleration and velocity pertaining to the toolpath, material deposition rate, the temperature of the material, the temperature of the bed in which the material is deposited, among others [4]. Although some instructions may

differ depending on the machine used, the creation of these instructions is a feature shared by all AM technologies [4].

2.2.1 Binder-jetting (BJ)

Binder-jetting is an additive manufacturing technology initially developed by the Massachusetts Institute of Technology in the 1990s [5], and later commercialized in 2010 [6]. This technology is able to manufacture parts from materials including sand, glass and metal. The entirety of the BJ printing process can be divided as follows: printing, curing, de-powdering, sintering, infiltration, annealing and finishing [6]. The printing process is the most distinguishable feature of binder jetting. The printer consists of a powder bed (on which the part is printed on), a powder dispenser, and a binder material dispenser. Every layer begins with a thin powder spread over the powder bed, then depending on the layer-by-layer instructions for that respective layer, powder binding material is deposited. When all the layers have been deposited, the material is then post-processed to remove unwanted material in such a fashion that only the material on which the binding material was deposited on remains, and thus the part is created. Today, binder-jetting technology is a widely used and commercially popular category of additive manufacturing, due in part to the advantages that it provides the user, such as an ample range of printing materials and ease of use. However, BJ faces the challenges of long post-processing times, and finished products that may not be suitable for industrial structural applications due to the porosity intrinsic to the nature of the printing process. In this process, the mechanical properties of the finished product fall short when compared to the other additive manufacturing categories [7].

2.2.2 Directed Energy Deposition

Directed Energy Deposition (DED) is an additive manufacturing process in which focused thermal energy is used to fuse materials by melting as they are being deposited [1]. The thermal

energy sources to fuse material can be varied, including laser, electron beam, or induction heating, among others [8]. This AM technology was developed by Sandia National Laboratories in 1995 and was later commercialized by Optomec [9]. The DED technology consists of a nozzle mounted on a multi-axis arm, through which material is deposited onto a surface and being fused together at the same time [4]. The nature of the technology allows versatility of materials – being compatible with polymer, ceramic, and metallic use, the latter being the most prevalent. The system is also enabled to be wire-fed or powder-fed. The advantages of DED are its compatibility with multiple materials and its ability to double as a repair tool to fix localized damage in a part [9]. Some of the current areas of investigation for DED technology are related to the distortion and residual stresses caused by the temperature dynamics experienced during the manufacturing process [10].

2.2.3 Material Extrusion (ME)

Material extrusion is an AM process in which material is selectively dispensed through a nozzle or orifice [1]. Currently the most popular technology on the market, accounting for 40% of all produced parts [11], ME is similar to other AM technologies in the preprocessing steps. However, the printing process works through the liquification of material inside a barrel, extruded by pressure through a nozzle into a surface according to any given two-dimensional toolpath. The barrel system and nozzle are conventionally referred to as the print head. Once the material is deposited into a printing bed, the material solidifies. Subsequent deposited layers are attached to the underlying substrate to add a third dimension to the part [4]. Because of the nature of the printing mechanism, polymers are the material best suited for this technology – particularly ABS [12, 13]. Common particular technologies that belong to this extrusion category are Fused Deposition Modeling (FDM) and Big Area Additive Manufacturing (BAAM), both of which will

be further covered in extensive detail. Recent research efforts have been focused on improving the dimensional accuracy and print resolution, controlled extensively by a myriad of design and printing parameters ranging from the extruder temperature, the velocity at which material is deposited, and the velocity of the gantry system on which the nozzle is mounted on [11]. Other problems include poor geometrical accuracy due to deformation or warping caused by residual stresses related to material temperature.

2.2.4 Material Jetting (MJ)

Material jetting is an additive manufacturing process in which droplets of build material are selectively deposited [1]. This technology works in a similar fashion to conventional two-dimensional print that most readers are familiar with – i.e. a regular paper printer to print documents. The printing process of MJ deposits a layer of material in the shape of liquid drops on a surface, or bed, where the material solidifies prior to deposition of the next layer. As the new layers are stacked up, the part is formed in three-dimensions. This process is similar to BJ, except the binder substrate and the filler material are deposited in a simultaneous fashion through the nozzle. Due to the nature of the complexity of this printing process, MJ is most commonly used with polymer materials, but can also be used with metals and ceramics [4]. The de facto challenges that MJ technology is facing today are the formulation of the liquid material used for printing, the material droplet formation, and the control of the deposition of the droplets [4, 14].

2.2.5 Powder Bed Fusion (PBF)

Powder bed fusion is the additive manufacturing process in which thermal energy selectively fuses regions of a powder bed [1]. This printing process works in a similar fashion to BJ, in both systems a fine spread of powder is deposited in every layer, and then the respective portion of the powder that corresponds to the layer of the part is bound together. In the case of

PBF, the powder is bound by thermal energy coming from a laser beam [4]. This additive manufacturing category works exceptionally well with metals. Although initially this technology was used for rapid prototyping of metal parts, today PBF can produce parts at over 99.5% of the full density obtained with conventional metal production methods – thus becoming one of the most promising technologies to be adopted by the automotive and aerospace industries [15]. This technology is still being optimized to this day, with the biggest challenge deferring it from the introduction to the broader market is the uncertainty of the quality of the final product. Research is being conducted today to gain familiarity and expertise with the process parameters in order to obtain a consistent final product quality [15, 16, 17].

2.2.6 Sheet Lamination

One of the first commercialized additive manufacturing techniques [4], sheet lamination is the additive manufacturing process in which sheets of material are bonded to form an object [1]. In other words, following the preprocessing step of having the CAD model be divided into multiple two-dimensional layers, than when stacked form the full three-dimensional part, in sheet lamination layers of material are precut corresponding to a respective layer dimensions. These layers are then stacked and bonded together whether by an adhesive bonding, thermal bonding, clamping or welding mechanism [4]. This process drew interest from several industries, particularly in the creation of tooling for forming manufacturing, e.g. hydroform tools and stretchform dies [18, 19]. The advantage of this process is the variety of materials that can be used to fabricate a part, the ability to create internal geometries, and the intrinsic simplicity of it - i.e. low temperatures, low energy consumption, etc. – which make it ideal for making rapid prototypes for visual aid purposes [13]. However, one of the main challenges that this technology faces is the

delamination between the surfaces [18], limiting the use of this technology from high tensile purposes, ergo the use in tooling applications requiring manufacturing by compressive stress.

2.2.7 Vat Photopolymerization

Vat photopolymerization is the additive manufacturing process in which liquid photopolymer in a vat is selectively cured by light-activated polymerization [1]. In other words, the part undergoes a similar preprocess to the aforementioned AM categories, except for every layer of this material, a liquid is placed in a two-dimensional shape, which solidifies upon contact with radiation, usually in the ultraviolet (UV) wavelength range [4]. Usually the materials for this process are precisely chemically developed to react to UV light, commonly polymers. This AM category is popular in the tissue engineering field due to its ability to create large parts with sub-millimeter details [20, 21]. Some of the prominent topics in the research field are the creation of complex polymers that adhere to the UV radiation parameters present during the printing process.

2.3 Material Extrusion Technologies – An Overview

Because of the author's research focus on material extrusion technologies, a more in-depth overview of the material extrusion AM category will be presented, along with a detailed description of FDM – the most prominent expression of ME – and BAAM – the central subject of this thesis [12]. The mechanism of operation of these technologies, the compatibility of materials, and the current challenges faced by their respective industries will be described. As previously mentioned, material extrusion additive manufacturing works through extruding semi-molten material through a nozzle onto a surface according to a specified two-dimensional tool path. The material then solidifies and a subsequent layer is then deposited on top. This process is repeated iteratively until the three-dimensional part is complete. The layers are conventionally named by increasing number, layer 1 being the bottom-most layer. In addition, the coordinate system

globally referenced and used in ME technology is illustrated in Figure 2.1 below. The z-axis is perpendicular to the printing bed, parallel to the extruder nozzle, the x-axis is along the longer side of the printing bed, and the y-axis is along the shorter side of the printing bed.

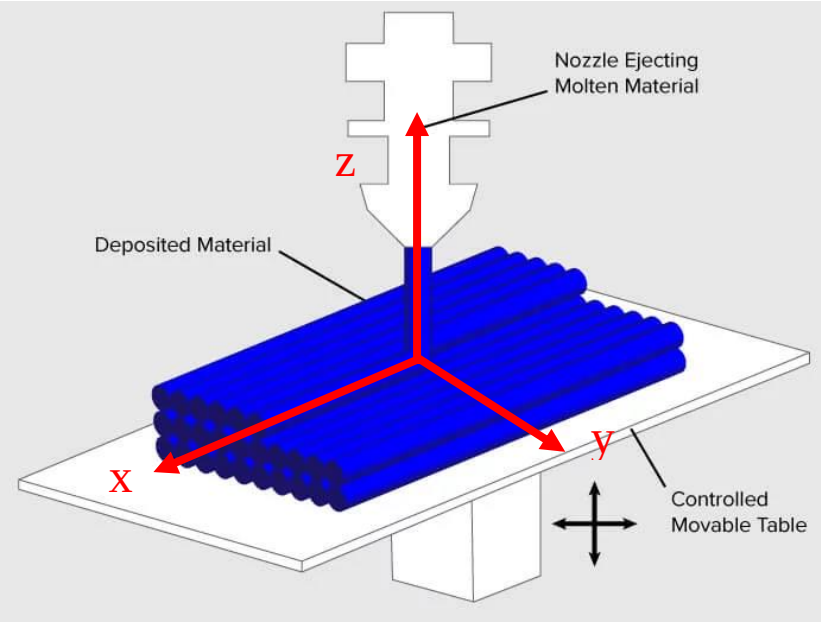

Figure 2.1 A schematic of an approach to the material extrusion process. Notice the conventional coordinate system, in red, used in this technology [46].

2.3.1 Polymer Adhesion in Material Extrusion Process

This section describes the mechanisms behind the adhesion of ABS filaments during the material extrusion process. As previously discussed in the FDM section, the material is extruded in a semi-molten state in to a build platform, the material solidifies and then a new semi-molten layer of material is added. The structure is only allowed to be built up because of the adhesion between substrate and new layer. In a work conducted by Li, he describes this sintering – the bonding formation process in the FDM process – in detail [22]. This sintering is driven by the thermal and surface energy stored in the semi-molten filaments in four steps: 1) Initial Contact, 2) Wetting, 3) Diffusion, and 4) Randomization. . The first step in the sintering process is the contact

between filaments, instantly followed by wetting. In the wetting process, the molecular contact at the interface causes the interface barriers to disappear as these two filaments merge into one in a process called diffusion. The wetting and diffusion processes have a large impact in the strength of adhesion of the material, as the larger the contact area is, the stronger potential adhesion strength will be. In some materials, this diffusion process is followed by a randomization step, where both filaments become one enlarged piece with indistinguishable barriers between them. In the case of ABS, printed with the BAAM machine, the randomization process seldom occurs at conventional printing temperatures [23]. It is important to notice that in temperatures above 290 C, the material spread over the bed – this phenomenon was attributed to the high viscosity caused due to the thermal oxidation degradation process in ABS [22]. In the BAAM printing process, efforts have been made to improve the adhesion between layers, through a tamper mechanism, intended to apply pressure on a newly deposited layer onto the substrate, and thus increasing the surface contact area and the neck section [24].

2.3.2 Fused Deposition Modeling (FDM)

Fused Deposition Modeling, or FDM, is an additive manufacturing technology invented, trademarked and commercialized by Stratasys, Inc., in 1992 [25]. It is also known as Fused Filament Fabrication (FFF). Today, Stratasys remains the leading manufacturer of extrusion AM systems [11]. The preprocessing steps for FDM are similar to any other AM category previously mentioned. However, the printing process is different. A filament feedstock is supplied to a heated barrel through an electric motor controlled pinch roller mechanism. In this barrel, the filament is heated up to a semi molten state, and then it is deposited through a nozzle onto a heated bed. The material is deposited in its molten state following a two-dimensional toolpath specific to that layer.

The material then solidifies and a subsequent layer is deposited on top of this substrate, thus adding the third dimension of the solid model into the print.

FDM is exclusively used with thermoplastic materials, including but not limited to acrylonitrile butadiene styrene (ABS) in several variations, Agilus30, Antero 800NA, ASA, Durus, Nylon in several variations, polycarbonate (PC), Tango, ULTEM, and Vero [26]. Among these, the most prominent and prevalent used in conjunction with FDM is ABS [11]. In a later section, due to the importance of ABS in the AM industry, but most importantly being the material used in this research, an in depth review of ABS will be conducted.

As previously mentioned, recent research conducted in [11] demonstrate the importance of dimensional accuracy, resolution, and surface roughness to improve the position of FDM technologies in the broad market – expanding its way more away from visual demonstrations into industrial applications where FDM fabricated parts are comparable in meeting the requirements as conventionally fabricated parts. In Turner *et al*., it is stated that the toolpath parameters in the product design, the liquifier and environment temperatures and cooling rate, as well as the process control algorithms, regarding the filament feed rate, are the most important factors to keep in mind when trying to improve the aforementioned quality specifications [11].

Currently, the maximum feature resolution that obtainable with ME systems is 100 micrometers [11]. The best way to improve resolution is through improved control algorithms, process monitoring capabilities, and process feedstock specifications – parameters usually not controlled by the user, but rather embedded into the software. The thermomechanical properties of the feedstock material also play a role, and not enough research has been conducted, or disclosed, regarding these – this problem is one of the most prevalent problems in Big Area Additive Manufacturing, further discussed in this document. As far as surface roughness is

concerned, Turner *et al.* concluded that there remains a need for strategies to optimize surface finish and the need for post processing of a part. Current research is being performed in that [11].

2.4 Big Area Additive Manufacturing (BAAM)

The Big Area Additive Manufacturing (BAAM) thermoplastic extruding machine was developed by Oak Ridge National Laboratories (ORNL) and commercialized by Cincinnati Incorporated (CI) in the year 2015 [23]. The machine has a maximum print envelope of 240 inches by 90 inches by 72 inches, with a maximum feed rate of 80 pounds per hour. This large print envelope, as well as the higher throughput of material stand to benefit the aerospace and automotive industry, among others, through an increased production efficiency, which in turn can also be translated to lower production costs [27]. The aforementioned advantages make the BAAM thermoplastic extrusion machine a primordial subject of research.

The BAAM machine consists of a material feeder, which pulls the pellets from the stock and into a heated extruder, a heated single-screw extruder with a nozzle (diameter can be 0.2, 0.3, and 0.4 inches), fixed to an aluminum honeycomb gantry driven by linear motors with absolute positioning accuracy of +/- 0.005 inches, a tamper that taps the deposited bead to improve inter-layer adhesion in all directions [24], a heated bed in which material is deposited on, and a computer where the user can monitor and control the parameters used for printing. All of these components are supported by a steel plate fabricated frame. In addition, the BAAM thermoplastic machine is commonly used in conjunction with an attached material dryer, where the pellet humidity is removed prior to the start of the printing process. A compressor is also needed, since air pressure is the working mechanism driving the transportation of material pellets from the dryer into the extruder.

The machine works conceptually in a similar fashion to conventional FDM systems, as described above. The main difference in the operation is that the feedstock for the BAAM is not a filament, but rather material pellets that are fed into a heated single-screw and melted together to be deposited through a heated nozzle. Figure 2.2 below shows the described BAAM components.

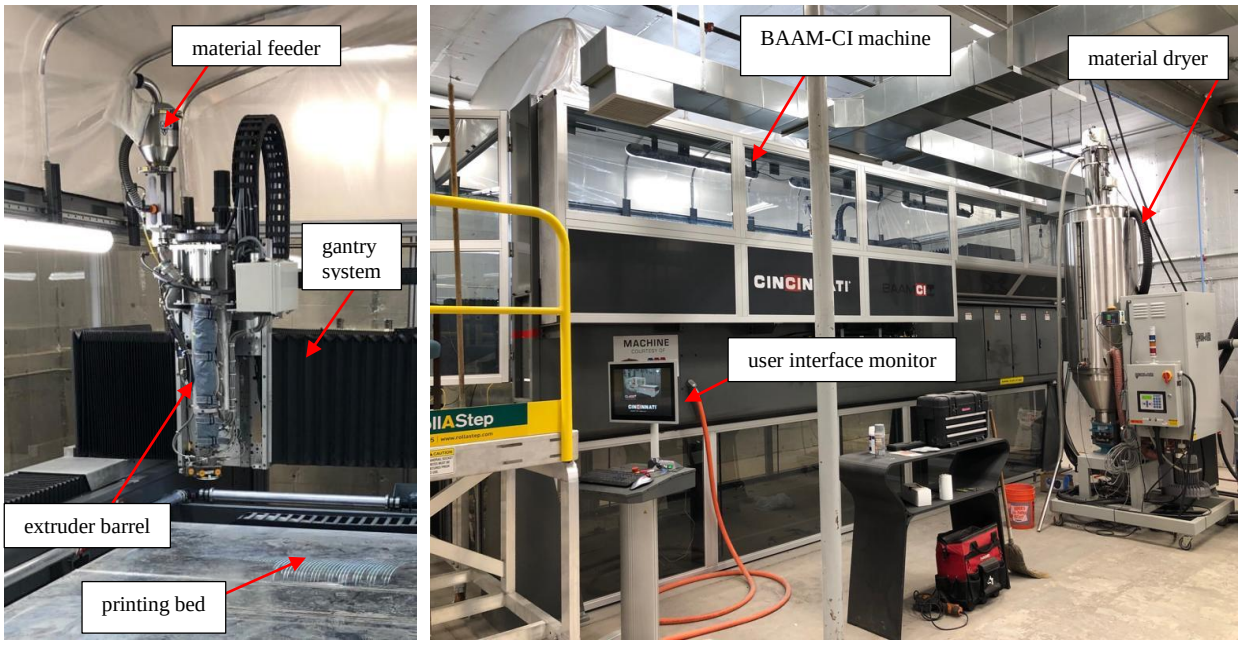

Figure 2.2 The BAAM-CI thermoplastic extruding machine, showcased with its components and appendages.

The BAAM extruder machine is most commonly used for the additive manufacturing of thermoplastics, including acrylonitrile butadiene styrene (ABS), PPS, PC, PLA and PEI – many times mixed with carbon fiber (CF) or glass fiber (GF) with the purpose of improving strength and thermal stability [28].

The thermomechanical properties are one of the most important factors that contribute to the dimensional accuracy of an AM printed part. According to [11], as the equipment becomes larger, the thermal gradients that occur in the printing process and their impact on the geometrical dimensions and their fidelity to the CAD model dimensions become compromised and therefore are increasingly important. Hence the focus of the thermomechanical properties and their

relationship to print quality in BAAM [11]. Also, according to Compton *et al*. and Gibson *et al*., the lower bound of the temperature leads to defects such as warping and cracking, however, the upper bound leads to poor adhesion between layers [4, 23]. The work by Gibson *et al*. suggests that it is because of the high temperature effect on flow conditions, which affect adhesion between layers [4]. This is investigated later in this document.

2.4.1 Current BAAM Research

As mentioned before, the BAAM thermoplastic extruding machine, with its promising advantages to the aerospace and manufacturing industries, is a prominent subject of research today. BAAM research is trying to tackle some of the same issues present in FDM systems, i.e. increasing dimensional accuracy, improving the surface finish, and improving inter-layer adhesion. In addition, being a new technology, BAAM is also facing problems outside of conventional material extrusion systems related to its fast deposition rates and high printing volume capabilities, which make heat transfer, dimensional control, and inter-laminar strength to be more challenging [2, 3, 23, 24]. The high extrusion rates, combined with the inherent nature of the screw extruder of the BAAM, make it difficult to predict the amount of material deposited, especially in sharp curve features, which result in varying bead dimensions. As such, it is harder to manufacture sharp geometry features (e.g. a uniform fill). Temperature is among the most prevalent challenges that BAAM is facing today, as previously mentioned, due to its inseparable relationship with inter-layer adhesion, as well as warping and cracking defects, sagging, and overall print quality [2, 22, 23]. Figure 2.3 below illustrates examples of some of the BAAM challenges.

Figure 2.3 Defects in BAAM printed parts. Frame (a) shows a gap between layers (red square), caused by temperature differences during deposition. Frame (b) shows a deformed infill, mostly noticed along the corner (red square), due to inconsistent deposition rates. In frame (c), the geometry of the part caused the shear force from the extruder, as it moved away, to unstick the deposited layers.

2.5 BAAM Materials

The central focus of this document is in the investigation of thermomechanical properties of parts printed with the BAAM-CI thermoplastic extruding machine, in particular, those printed with carbon fiber (CF) reinforced acrylonitrile butadiene styrene (ABS). However, the BAAM thermoplastic extruding machine can also be used in conjunction with dozens of materials, including polyphenylene sulfide (PPS), polycarbonate (PC), polylactic acid (PLA), and polyethylenimine (PEI) [28]. A brief summary of the thermoplastic material characteristics used with BAAM will now be presented, with a focus on amorphous thermoplastics and composites, as well as the description of their rheological properties and behavior, and concluding in an in-depth review of ABS, its origin, properties, utility, and challenges.

2.5.1 Amorphous Polymers

The materials used in conjunction with the BAAM-CI thermoplastic extruder machine fall mostly into the category of amorphous thermoplastics. A polymer is made of repeating chains of structural molecular units. Amorphous polymers have a random molecular organizational structure. This stands in contrast with crystalline materials – whose molecular structure is organized in patterns – and other materials such as metals – who also have patterns in their molecular structure, e.g. Face Centered Cubic (FCC), Body Centered Cubic (BCC), etc. The most significant property of amorphous polymers, vis-à-vis additive manufacturing, is a property defined as glass transition temperature (T_g).

Unlike crystalline polymers, with an increase in temperature, amorphous polymers don't transition from a solid into a liquid molten state, but rather transition from a solid glassy state, into a leathery state, then into a rubbery state, and finally into a rubbery semi-molten flow region – further described in the following section [29]. The glass transition temperature (T_g) is defined as the temperature where polymer chain mobility commences. The T_g is characterized as the threshold temperature that separates an amorphous polymer from being in a solid, glassy state (below T_g) from a rubbery state (above T_g). The glass transition temperature is one of the most significant properties in the Material Extrusion category of additive manufacturing, not only because it dictates the temperature at which printing can be made, but it can also be used as a guideline for predicting the structural integrity of a part, and thus preventing defects such as delamination, warping and cracking [23]. In other polymer manufacturing techniques, such as injection molding [3], the T_g also dictates the operating temperatures – printing at 120 °C above this threshold is the conventional practice. The T_g varies from material to material, and for

different material compositions. Now a brief overview of fiber composite materials will be presented, followed by a detailed description of ABS – the main focus of this investigation.

2.5.2 Fiber Composites

The integration of fibers to a matrix of material results in a material with higher strength, stiffness, corrosion resistance, and fatigue life, among other properties, in most occasions maintaining a relatively low weight compared to metal materials [30]. Because of the benefits of fiber composites, specifically their light weight, their development and use is of high interest for the aerospace, military, space and automotive applications. Although the introduction of fiber composites to the AM industry, there are still challenges present in this technology. These challenges include void formation, poor adhesion of fibers and matrix, and in some cases, blockage due to fiber inclusion, among others [31].

In FDM, fiber reinforcement has been a popular subject of research. Many efforts in FDM technologies have been directed to increasing the mechanical tensile strength of the material; glass fiber reinforcement in polypropylene (PP) increased the modulus and strength by 30% and 40% respectively [31]. Additionally, the addition of 30% short carbon fiber by weight to ABS, showed a 115% increase in strength and a 700% increase in Young's modulus, even surpassing the specific strength of aluminum. Continuous fiber reinforcement would improve the mechanical properties even significantly higher, but it is one of the biggest challenges researchers face today in the AM of composites. Regardless of the drawbacks, the additive manufacturing of fiber composites make it a respectable contender for production manufacturing, as opposed to just rapid prototyping. As far as BAAM fiber composite manufacturing, despite an increase in porosity and increased anisotropy, the tensile strength of the material was increased in the direction of print by 57% [24].

2.5.3 Acrylonitrile Butadiene Styrene (ABS)

ABS is an amorphous thermoplastic material with the chemical formula $((C_8H_8)(C_4H_6)(C_3H_3N))_n$. As the name indicates, acrylonitrile butadiene styrene is composed of acrylonitrile, butadiene, and styrene. The nitrile provides the material with glassy properties, and the butadiene provides the material with rubbery properties. ABS is a polymer that is widely used in the construction, personal care, toy, computer, and automotive industries because of its mechanical properties, chemical resistance, ease of processing and recyclability [32]. ABS can be used neat, although it is not uncommon to use ABS, or other thermoplastics, with fiber reinforcements to enhance their mechanical properties [31, 33, 34, 35].

ABS has a T_g of 105 °C, and a degradation onset temperature of 310 °C – both properties independent of the fiber reinforcement content [3]. ABS is able to hold its glassy mechanical properties when maintained under 80 °C, thus making it a popular material available for everyday commercial use, e.g. toy construction blocks. Although initially ABS was developed for use in injection molding, it has become a widely used material in the additive manufacturing industry because of its relatively low processing conditions and high impact resistance [32].

2.6 Rheological Properties in Amorphous Polymers

Amorphous polymers have viscoelastic properties. Rheological studies conducted on polymers intend to characterize the viscoelastic properties of materials. In the case of amorphous polymers, they transition between regions where elastic properties are more prevalent, and regions where viscous properties are more prevalent [29]. The rheological regions are the 1) glass, 2) leathery, 3) rubbery plateau, 4) rubbery flow, and 5) liquid flow. In the glass state the material behaves like a glassy solid. In the leathery region, the material becomes more malleable, and is able to deform without breaking. The transition between the glassy region and the rubbery plateau

is called the glass transition, triggered by the previously mentioned glass transition temperature (T_g). In the rubbery plateau the material has rubbery properties. In the rubbery flow region, the material is dominated by the viscous properties and is more prone to deformation and flow. Finally, in the liquid flow region, the materials flows akin to a liquid – this is typically the material state at which printing is performed [29]. The curves pertaining to the storage modulus and the tan(δ), reflecting the transition in viscoelastic properties as a function of temperature and shear rate are depicted in the Figure 2.4 below.

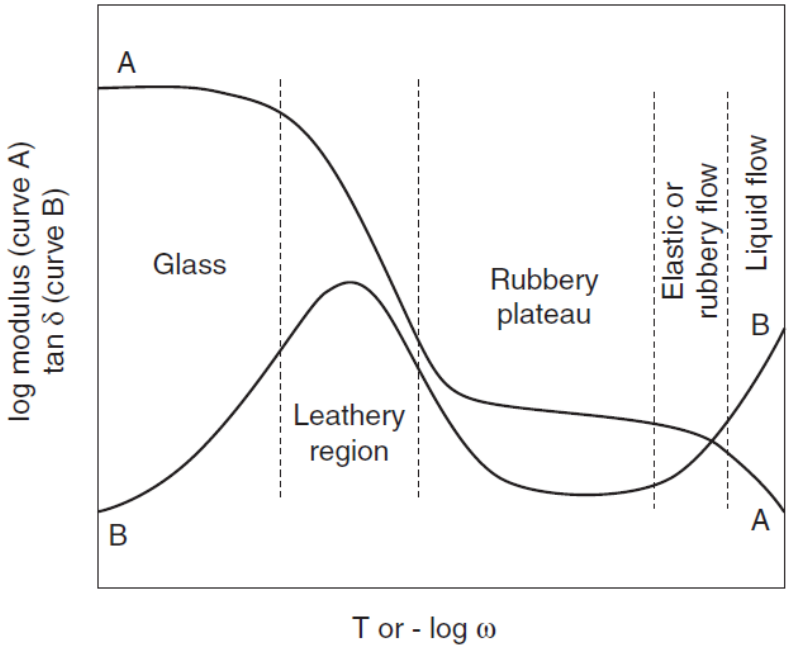

Figure 2.4 The tan(δ) and storage modulus curves for an amorphous polymer, showcasing the different regions at which a polymer has distinct viscoelastic properties [31].

The storage modulus corresponds to the elastic properties in the part, i.e. its resistance to plastic deformation when subjected to a load. The tan(δ) represents the ratio of the loss modulus (E'') over the storage modulus (E'), seen in equation 1 below.

$$\tan(\delta) = \frac{E''}{E'} \qquad (1)$$

The tan(δ) ranges from zero to infinity, the former being the value for an ideally elastic material, and the latter being the value for a perfectly viscous material. A perfectly elastic material would have no energy losses (E''= 0), because the material would "bounce back" with an elastic response equivalent to the energy put in, e.g. a perfectly solid glass ball dropped from a height bouncing back to the same height. On the other hand, a perfectly viscous material would have no storage modulus (E' = 0), resembling liquid water dropped from a height onto the ground and deforming on contact. To illustrate this concept, Figure 2.5 below is the dynamic graphical representation of the storage and loss modulus in a bouncing ball.

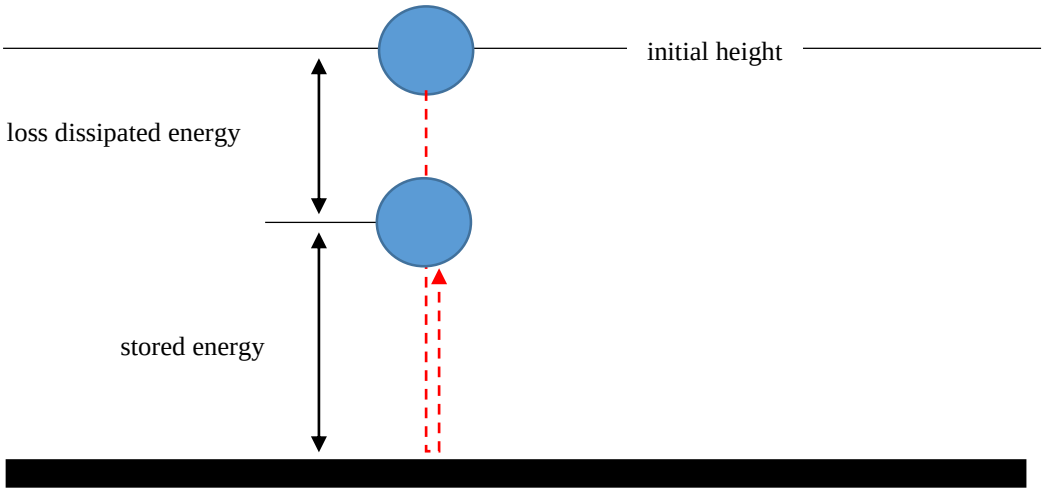

Figure 2.5 Visual representation of the storage and loss modulus in action. Notice the storage modulus (E') indicates of the energy used to bounce back and the loss modulus indicates the energy lost as heat (E'').

The angle, δ, represents the lag between an applied strain and the responding stress of the material. For instance, a perfectly elastic object would immediately react to an applied strain, and thus the angle representing the lag would be zero degrees. On the other hand, a perfectly viscous object would have a lag angle of 90 degrees between the strain and the response stress.

2.7 Compression Testing

Compression testing is used to evaluate the behavior of a material under a compressive load. Compression tests provide us with several material properties that are relevant to its characterization, and ultimately identify appropriate uses for it. Among the information obtained from the compression testing are the compressive load, stress, strain and displacement, from which the maximum load withstood prior to rupture, maximum load withstood prior to plastic deformation, and elastic modulus, among other properties, can be obtained. It is performed on a wide range materials, including metals, ceramics and polymers – each having its own set of official and universally recognized instructions set by ASTM International [37]. For instance, for the experimental methodology vis-à-vis compression testing conducted in this research, the ASTM D695-15: Standard Test Method for Compressive Properties of Rigid Plastics served as the set of guidelines and instructions for testing, delineating the test parameters to set in the appropriate testing machinery.

Compression testing is a well-documented testing method for assessing the behavior of materials under a load, identifying different compressive behaviors for different materials and material structures. Relevant to this research is the compression of structural foam materials, in which three regions were identified in the compression curve: 1) elastic, 2) crushing and 3) densification. The elastic region corresponds to the region where a material withstands load without suffering from permanent deformation, the crushing region corresponds to the region where the porosity in the material collapses, and the densification region corresponds to the region where the material, now pore-free, withstands its final load before rupturing [38]. In addition, with the integration of fibers into polymers, i.e. the creation of composite materials, the changes in compressive behavior have also been evaluated to examine the effects of fiber loading on

compressive properties. Adequate testing methods for compression have also been evaluated to find the most suitable for composite materials, depending on the focus of the research [39, 40].

2.8 Infrared Thermal Scanning

With the introduction of additive manufacturing technologies that have a high dependence in heat control, temperature measurement is an essential tool to ensure a high print success and quality, as well as an important mechanism to understand the relationship that temperature has with a wide variety of properties in different materials and processes. In the case of temperature dependent material extrusion processes, because of the previously described nature of the process, it is not feasible to apply contact temperature measurement techniques (e.g. to interrupt a material extrusion printing process to insert a thermocouple or thermometer in a part would disrupt the temperature control of a part, and may result in warping or cracking defects). The importance of temperature control for the successful printing using material extrusion systems, including the BAAM thermoplastic extruding machine (the focus of this work) has been discussed in the previous sections. Infrared Thermal Scanning, also known as thermal imaging or IR thermography, is an in situ method of recording the temperature of an object without having the need to have physical contact with it [41]. Thermal imaging is a well-documented and valid non-destructive evaluation technology used in the research of thermoplastic and composites [41 - 44].

Infrared thermography works by detecting the infrared radiant energy emitted, depending in the specific material's emissivity. This energy is converted into a digital signal and presented in an image where the user can visually see the radiation energy gradient in a color spectrum, and the temperature reading of the object in every pixel. Every material has a different emissivity value, dependent on temperature, which must be inputted into the IR processing software to ensure accurate readings. In addition, the emissivity value varies from material to material, but it is also

affected by the object's surface roughness, material composition, camera angle, reflectivity of the surroundings, and the object's geometry [42]. It is important to notice that only when the previously mentioned parameters are accounted for in an IR measurement can a true absolute temperature be calculated. Otherwise, the data captured becomes a relative value.

Chapter 3

Experimental Methodology

3.1 Material

The material used here was carbon fiber reinforced (20% wt.) acrylonitrile butadiene styrene (Techmer Electrafil J-1200/CF/20 3DP, Techmer PM, Clinton, TN, US), henceforth referred to as ABS-20CF. The material was dried for 4 hours at 90 °C before printing. Single-bead hexagon and thin-wall geometries – later described in detail - were printed using a BAAM-CI 100 (Cincinnati Inc., Harrison, OH, US) large scale thermoplastic extruder machine located at the University of Texas at El Paso (UTEP). The machine deposited the material at a rate of 100 mm/s over a heated bed set to 110 °C using a 7.62 mm (0.3") nozzle. The printing temperature settings are shown in Table 1 below.

Table 3. 1 The BAAM temperature settings.

material	melt	barrel 1	barrel 2	barrel 3	barrel 4	tip 1	tip 2
ABS-20CF	225 °C	200 °C	215 °C	240 °C	240 °C	230 °C	225 °C

3.2 Emissivity

With the interest of obtaining absolute temperature measurements with an infrared (IR) temperature camera, the emissivity of the printing material was obtained experimentally at four different temperatures. A piece of ABS-20CF material, with dimensions of 4.33 mm by 11.73 mm by 8.76 mm, was obtained from a single-bead print and heated in an Instron 3119-600 temperature-controlled chamber (Instron, Norwood, MA, USA) at temperatures of 100 °C, 150 °C, 200 °C and 250 °C - temperatures within the conventional range of the ABS-20CF BAAM printing process [23]. The temperature of the piece as it was heated was recorded with both an embedded type-K thermocouple (GG-K-24-SLE-100, OMEGA Engineering, INC., Norwalk, CT, US), in conjunction with a NI-9214 terminal module, processed with the NI-Signal Express 2013 software

(National Instruments, Austin, TX, USA), and a FLIR-SC645 infrared (IR) camera, used in conjunction with the FLIR ThermaCAM Researcher Pro 2.10 Software, (FLIR Systems, Wilsonville, OR, USA). A single frame of the IR recording was analyzed and compared with the thermocouple reading at the same instant in time, for every temperature. Figure 3.1 below shows the experimental setup, as well as a sample IR frame.

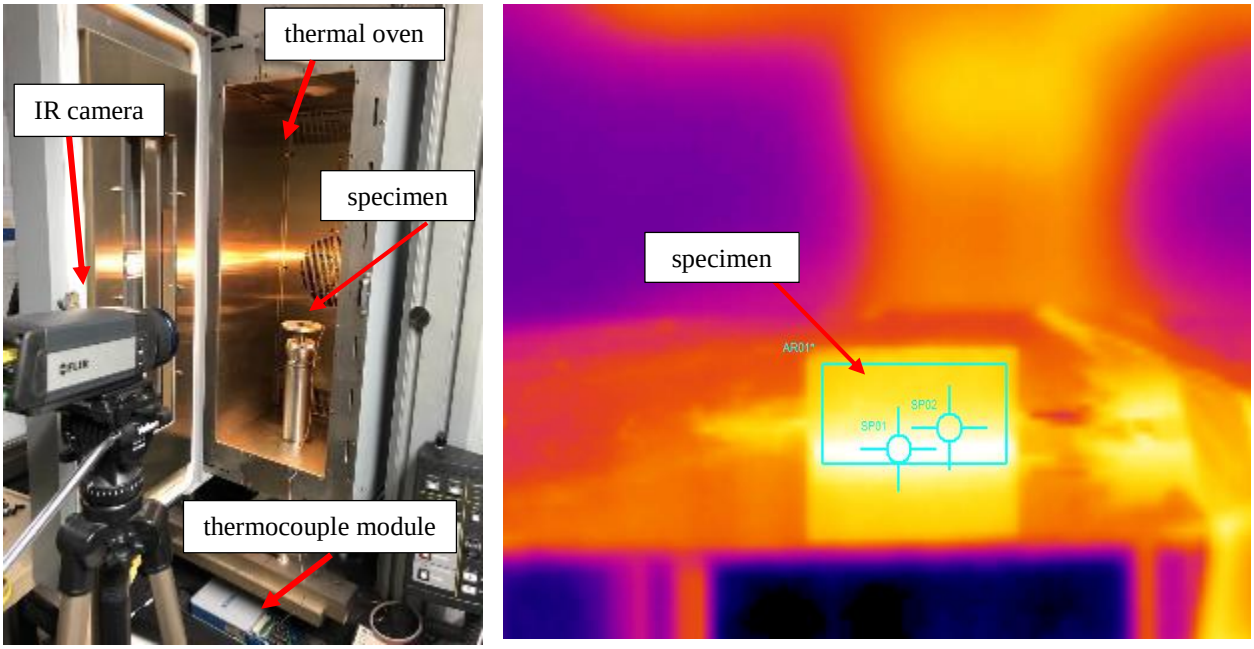

Figure 3.1 The experimental setup (left) and an image used for emissivity calculations (right).

The reader should note that the emissivity value used in this work was assumed constant and was determined experimentally (with the setup described above), accounting for variation in emissivity over a temperature range of 100 °C to 250 °C. The variation of emissivity in relation to surface geometry, and the impact of radiation from the surroundings on IR imaging were not considered. As a result, the reported temperature from the IR camera should be considered a relative temperature used to provide temperature feedback in the BAAM printing experiments.

3.3 Hexagon Prints

Two single bead, 13-layer hexagonal geometries were printed using a BAAM-CI large scale thermoplastic printer using ABS-20CF. Each wall of the hexagon measured approximately 130.40 mm (5.13 in), with an average bead width of 8.90 mm (0.352 in) and an average bead height of 3.70 mm (0.15 inches). One print was conducted without any waiting time between the end of a layer deposition and the start of a new layer deposition. In the other print, a 90 second standby time was added between layer depositions. Because the relationship between geometric features and failure would add a degree of complexity to the experiment and diminish the value in the 1-dimensional heat transfer model developed in this work (further described), it was concluded that the analysis of a single-bead wall feature was the most relevant for this research. However, the difference in print quality between these parts, illustrated in Figure 3.2, served as motivation to further investigate the relationship between substrate temperature and deformation. A frame of the IR analysis of the hexagon print can be found in Appendix C.

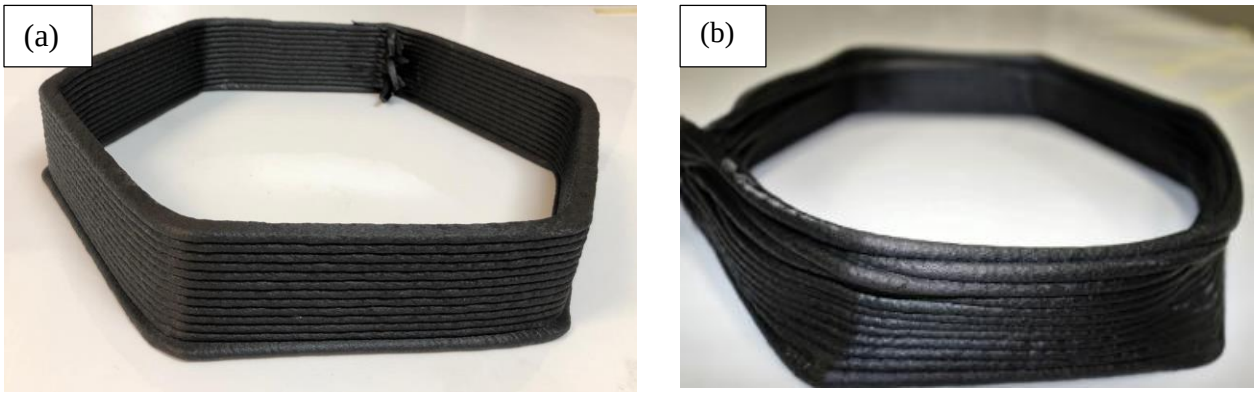

Figure 3.2 The hexagon geometries printed with the BAAM machine. Frame (a) depicts a hexagon printed with a 90 second delay between layers, while frame (b) depicts a hexagon geometry printed with no added layer time. Notice the difference in print quality where the part shown in (b) is defective.

3.4 Single-bead Vertical Wall Print

As described previously, a single-bead wall of ABS-20CF was printed with the BAAM-CI thermoplastic extruder to remove the geometry variable from the previous hexagon geometry print. A schematic of the wall can be found in Figure 3.3 below. The wall was 500 mm (19.685 in) in length, 11.81 mm (0.465 in) in width (a single bead width), and 62.23 mm (2.45 in) in height. A total of fourteen layers were printed, but the last two failed to adhere to the substrate.

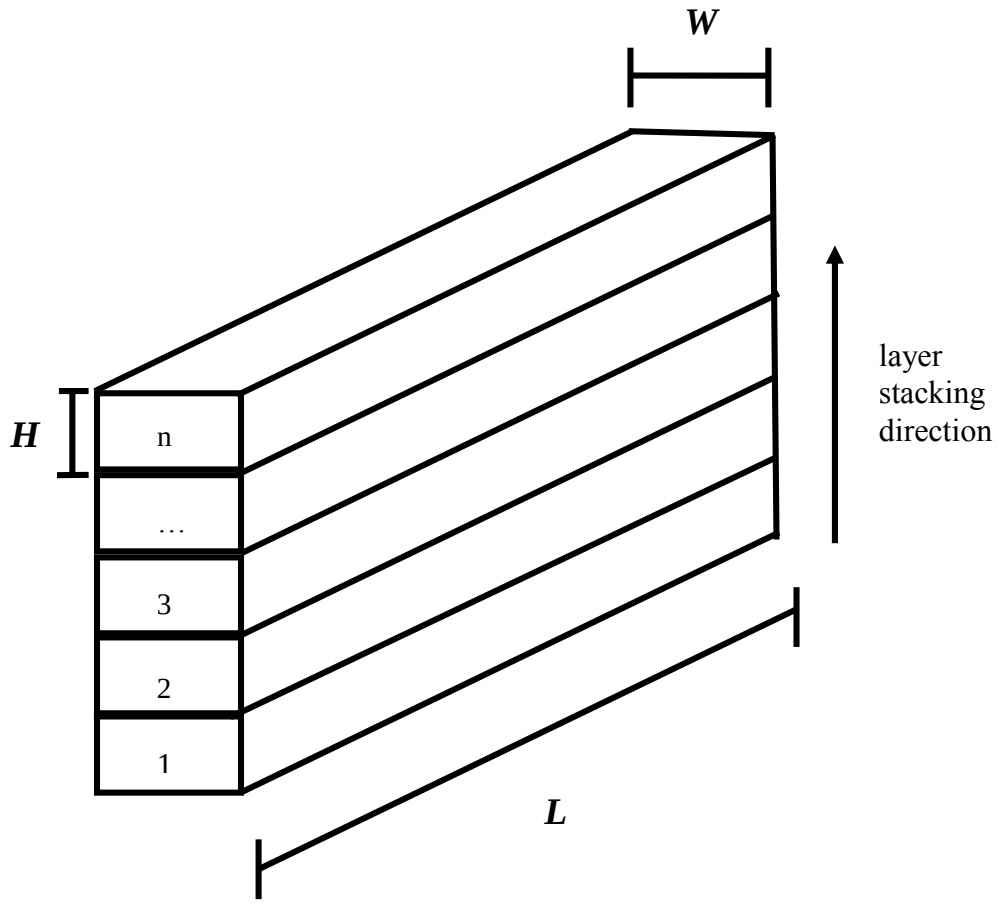

Figure 3.3 A schematic of the single-bead vertical wall print, where *L* is the length of the wall, *W* is the width and *H* is the height of a single bead.

Temperature data were collected with a FLIR D695 infrared camera, and processed with the ThermaCAM Researcher Pro 2.10 software. In addition to this, two more videos of the print

were recorded for visual analysis, one from the front of the wall, located across from the IR camera, and another from the side, perpendicular to the direction of print. The experimental setup for the thermal analysis and video recording is illustrated in Figures 3.4 and 3.5 below.

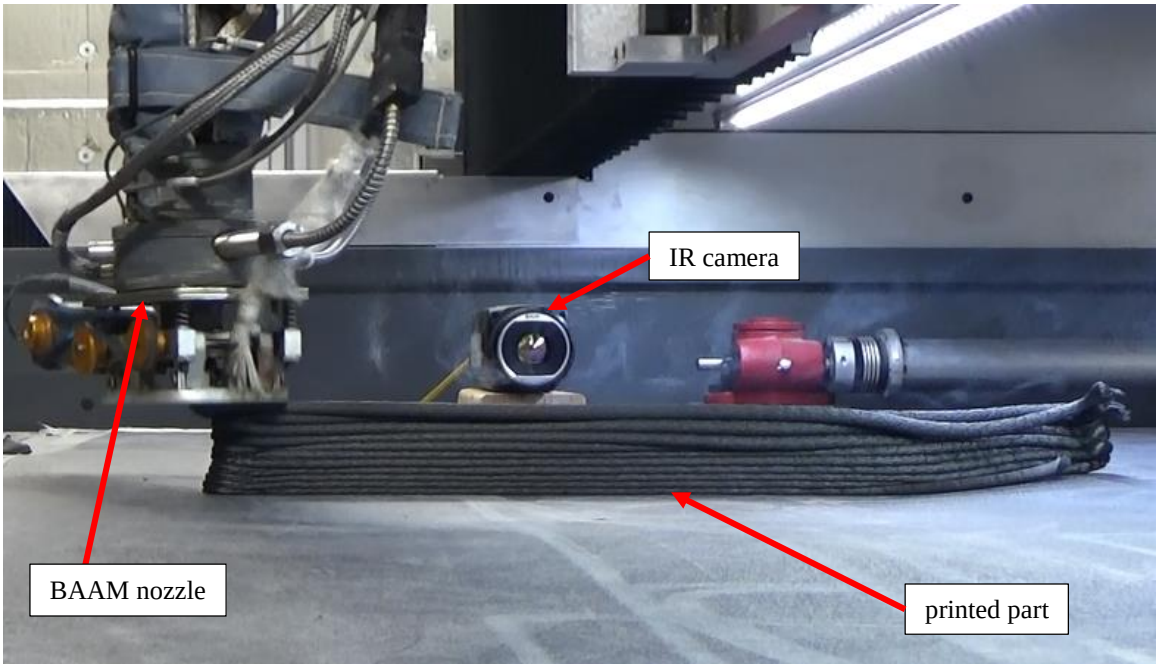

Figure 3.4 A frame of the video recording of the single-bead wall print, used to illustrate the experimental setup of the thermal analysis and video recording during the printing process.

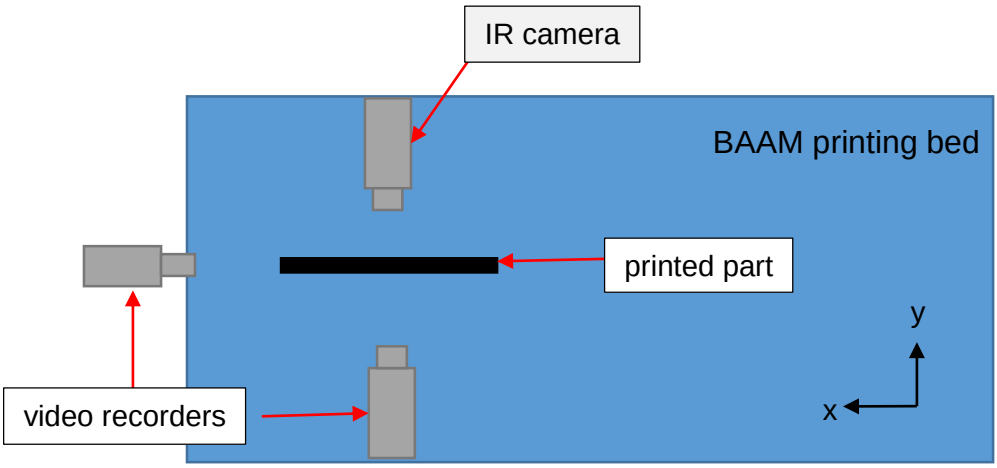

Figure 3.5 An illustration of the thermography and video recording setup during the printing of the single-bead wall feature, viewed from the top.

Furthermore, a frame of the thermal analysis, processed with the ThermaCAM Researcher Pro 2.10 can be seen below in Figure 3.6. From the thermal analysis, the temperature of every layer for the full duration of the print, as well as the highest temperature recorded in the entire substrate just prior to the deposition of a subsequent layer, and the highest temperature recorded in a layer just after deposition.

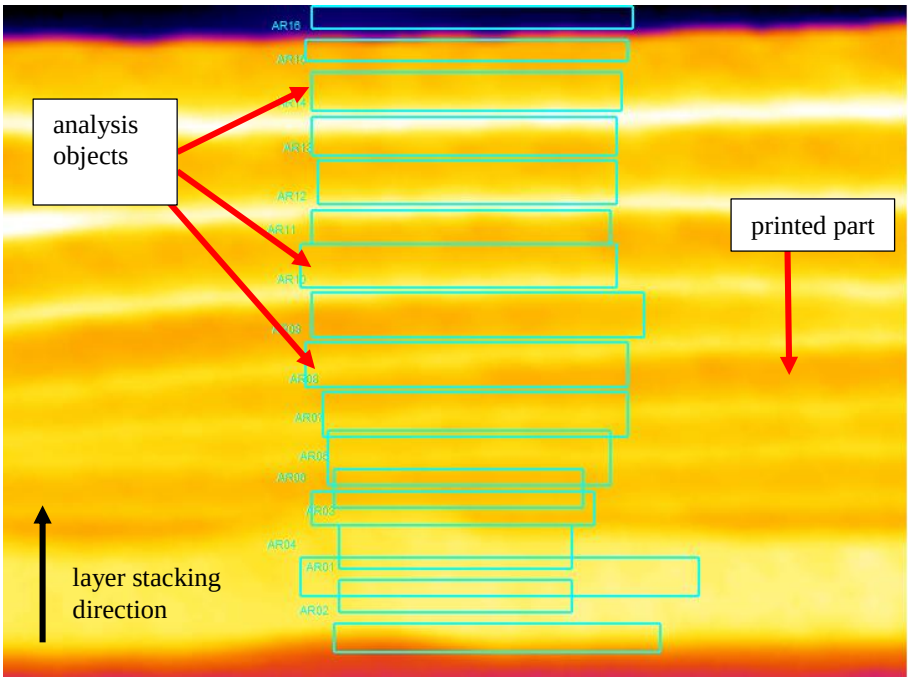

Figure 3.6 A single frame of the IR temperature analysis performed on the single-bead wall.

3.5 Experimentally Simulated Stress Deformation

As an inherent nature of the BAAM machine, high temperatures present in the substrate at the time of deposition lead to unwanted deformation of the part. In order to simulate real-life printing conditions, a single layer, single bead wall was printed. From this print, test specimens were obtained and used for compression testing under temperatures seen during a conventional BAAM print. The purpose of this single bead print is to evaluate the deformation of a single layer of material as a consequence of the added weight of the subsequent layer, at varying temperatures.

The tests were performed using the ASTM D695-15 standard to evaluate the compressive behavior of the printed carbon fiber reinforced plastic part [45]. The specimens were compressed at a rate of 1.3 mm/min in the z-direction until a strain level of ~60% was achieved. A total of fifty compression tests were performed under temperatures of 90, 110, 130, 150, 170, 190, 200, 210, 230, and 250 °C – five specimens tested at every temperature. These temperatures fall within the range seen in a conventional print from deposition to cooldown [23, 27]. It is important to notice that a printed sample with the recommended ASTM D695-15 dimensions would not accurately describe the compressive behavior of a single layer that this work intends to emulate. A specimen with the standard dimensions would have to be obtained from a multiple-layer print. Defects in the print that come from the multiple layer stacking, such as inter-layer porosity and delamination, would have been beyond the scope of this work. Therefore, to perform this compression testing, the test specimens were cut from a single bead, with average dimensions of 9.48 mm (0.37 in) by 10.87 mm (0.43 in) by 4.33 mm (0.17 in). The specimens were cut in an ATM Brillant 220 precision cutter machine, and the edges were grinded on an ATM Saphir 530 grinding and polishing machine (ATM GmbH, Mammelzen, Germany) to have an even, uniform, and burr-free definition. A schematic of the specimens obtained from a single layer bead can be found in Figure 3.7 below. A table with the recorded dimensions of every specimen, along with images of the experimental machinery used to prepare the specimens can be found in Appendix C.

Note that when performing the compression testing, the changes in cross-sectional area attributed to compressive strain deformation, imperfect shape of the sample, and losses in porosity were not considered when analyzing the compressive behavior of the samples. Rather, the cross-sectional area was assumed to be uniform and constant. For the purposes of this research, the

compressive behavior was obtained as a function of temperature in the form of a compressive stress-strain analysis and a compressive load-displacement analysis.

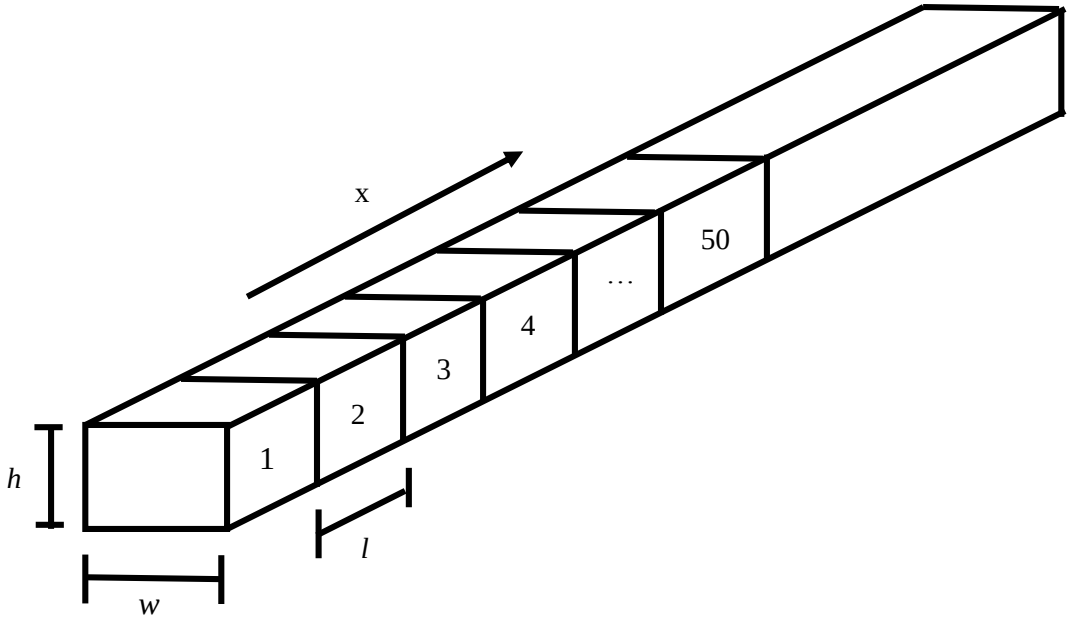

Figure 3.7 A schematic of the test coupons obtained from a single layer print.

The compression tests were performed using an Instron 5866 electromechanical testing machine used in conjunction with an Instron 3119-600 temperature-controlled chamber (Instron, Norwood, MA, USA). In order to monitor the temperature of the test piece with precision, a thermocouple was embedded into an untested sample piece, and placed inside the environmental chamber. Temperature readings were taken from this thermocouple to verify the tests were conducted at the specified temperature. The testing setup is depicted in Figure 3.8 below.

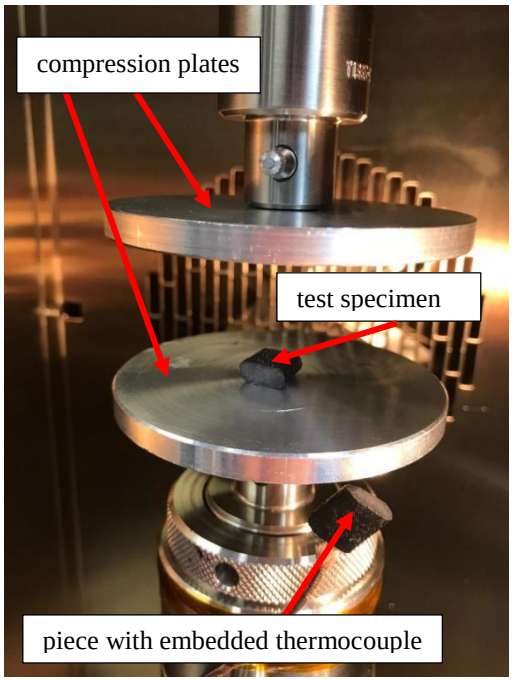

Figure 3.8 The experimental setup of the compression testing. The top compression plate moves down to exert a load on the specimen and bottom compression plate, which remain stationary.

3.6 Porosity

Optical imaging (5x magnification) was performed on cross-sections of the material that went through compression testing. The material was first cut using a precision high speed saw (Techcut 5, Allied High Tech Products, Inc., Rancho Dominguez, CA, USA) and were then mounted using a self-curing resin (Koldmount, MPC Industries, Albany NY US). The specimens were polished using 800-1000 grid papers followed by the use of a polishing pad with 0.05-micron alumina solution. An image of a specimen mounted in resin can be found in Appendix C. The as-polished specimens were viewed on a Keyence VHX-1000 digital microscope (Keyence Corporation of America, Itasca, IL US). Imaging analysis was conducted using Vision Assistant 2011 (National Instruments, Austin, TX, USA) by selecting a region of interest of known area and then extracting the Hue, Saturation, and Luminance colors (HSL). Then a darkness threshold was established where the voids would automatically change to red color, and the rest would turn black

due to the difference in the HSL spectrum. A particle analysis was performed on this binary file to determine the area covered by voids (red color). Finally, calculations were made to determine the void content of the samples at that particular area view. Note that in this work, the volume of voids is not being measured, instead the void percentage is being represented by the area the voids occupy within the bead's two-dimensional cross-section. As a method of ensuring the particle analysis is accurate, already certified copper powder with an average particle size of 60 microns was measured with Vision Assistant 2011. The software measured an average particle size of 63 microns, which means the software overestimated the measurement by about 5 percent. A frame of the analysis, for a sample compressed at 0.7 mm, illustrating the methodology of the processing software, can be found in Figure 3.9 below. The quantity of pores the software identified was verified visually.

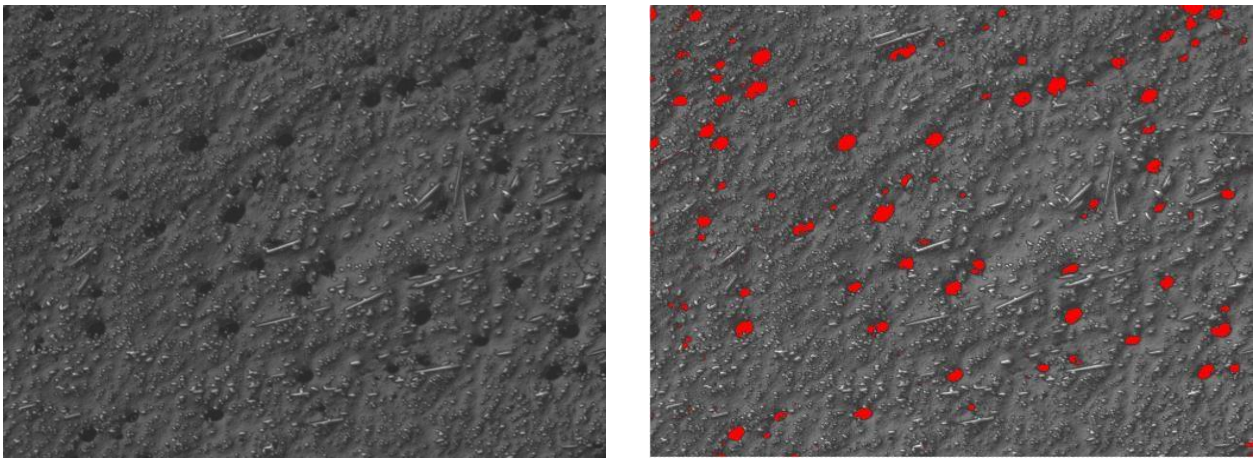

Figure 3.9 A frame of the porosity analysis performed with the Vision Assistant 2011 software. The original image is in the left, and the processed image is in the right. The red dots in the right image represent the pores found in the first image.

Four images were collected, from four sections identified during compression testing: 1) before compression, 2) initial compression, 3) plateau and 4) final compression. The side-by-side comparisons of the original image and the processed image for all displacement levels are found

in Appendix D. The four specimens used were compressed with an Instron 5866 electromechanical testing machine, at a temperature of 130 °C, until they reached a displacement of 0.2 mm, 0.7 mm, 1.0 mm and 1.2 mm. These displacements were chosen because they fall within the range of the four sections described above, as can also be seen in Figure 3.10 below.

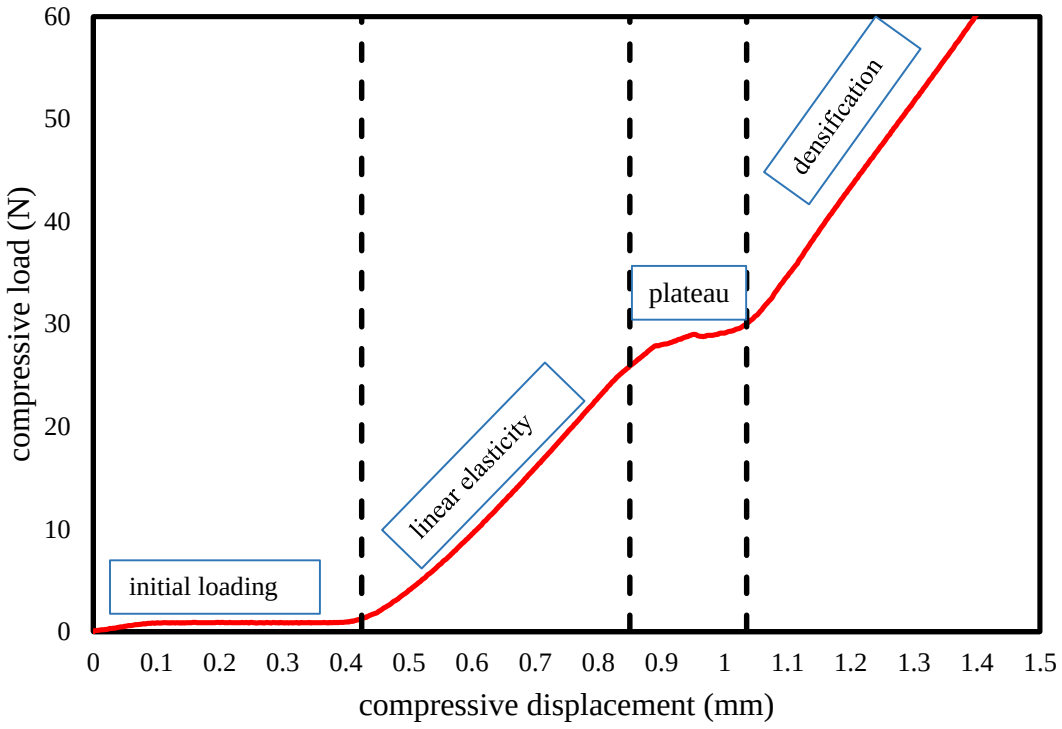

Figure 3.10 The different regions in the compression curve for ABS-20CF at 130 °C.

3.7 Rheological Testing

Dynamic melt rheology tests were performed according to the ASTM D4440-15 standard [46]. The goal of these tests was to evaluate the viscoelastic properties of the ABS-20CF material which dictate the printing parameters in fused filament fabrication. As the material goes through several thermal events with unique viscoelastic properties during the printing process [5], the temperature range for these tests was chosen based on the thermal history of the printed part. A

Discovery Hybrid Rheometer, DHR-2 (TA Instruments, New Castle, DE, USA) was used to perform the rheology tests of ABS-20CF pellets. In each test, a new batch of pellets was used to avoid the temperature induced properties in previously used materials. A total of eight tests were conducted at a temperature range of 160 °C to 230 °C, in intervals of 10 °C. The rheometer (DHR-2) was mounted with two parallel plates with a diameter of 25 mm, and a gap of 2.0 mm. The tests were conducted at a strain rate of 0.1% at a frequency range of 0.1-628 $rads^{-1}$. The tests were conducted in an air environment within the environmental chamber.

3.8 Final Prints

Following the compression testing and rheological analysis, two more prints were performed using the same printing parameters described in section 3.1, except for a newly introduced standby time between layer-depositions, used to control the temperature of the substrate just prior to the deposition of a new layer. The substrate temperature in prints A and B were maintained at 200 °C and 220 °C, respectively. The structural quality of the final prints was evaluated visually based on layer adhesion, presence of deformation, and overall structural integrity of the part.

In order to obtain the waiting time between layer depositions, the 1-D thermal model developed by Compton *et al.* was modified and implemented [23]. The material properties used in the Compton *et al.* model, outlined in Table 2 below, remained unchanged in this paper's model implementation. The thermal model equations and the MATLAB implementation can be found in Appendix C. Adjustments to the thermal model included the printing parameters used in the final print, the bead dimensions, and the desired layer temperature control. During the simulation, a temperature check was added at the end of every layer, by comparing the temperature of the top most layer against a set threshold temperature. For layers under the set value, the simulation was

set to continue as normal, but for values over the set temperature, the layer time was extended to allow for additional cooling time. In the end, the code would output an optimized layer time table to ensure that the top layer temperature remains below a threshold before deposition of a new layer. The temperature of the substrate during the final prints was monitored with a FLIR D695 IR camera and processed with the ThermaCAM Researcher Pro 2.10 software. A video recorder was also used to capture the entire printing process, and allow for visual inspection for deformation. The setup for the thermography and video recording are the same from Section 3.4.

Table 3. 2 The ABS-20CF material properties inputted in the 1D thermal simulation [23].

Variable name	Value
Thermal conductivity, k [W/m.K]	0.17
Specific heat capacity, c_p [J/kg.K]	1640
Glass transition temperature, T_g	110
Density, ρ [kg/m^3]	1140
Natural convection, h [W/m^2.K]	8.5

Chapter 4

Results

4.1 Emissivity

From the two measurements recorded by the IR camera and the thermocouple, via the ThermaCAM Researcher software, emissivities were calculated for ABS-20CF at temperatures of 100 °C, 150 °C, 200 °C, and 250 C and are reported in Table 3. Due to the low variance in values over the selected temperature range, an average emissivity value of 0.95 was used in the further experimentation of this research.

Table 4. 1 The emissivity values of ABS-20CF over at temperatures of 100 °C, 150 °C, 200 °C, and 250 °C.

temperature, T [°C]	emissivity, ε
100	0.98
150	0.94
200	0.95
250	0.94

As previously mentioned, the variation of emissivity in relation to surface geometry, and the impact of radiation from the surroundings on IR imaging were not considered. As such, the reported temperature from the IR camera should be considered a relative temperature used to provide temperature feedback in the BAAM printing experiments.

4.2 Hexagon Prints

The hexagon geometry printed without a waiting time between layers experienced deformation after the deposition of the fourth layer (Figure 4.1 below). In contrast, the hexagon geometry with a 90 second standby time between layers was successfully printed without any noticeable deformation. However, although the geometry held its shape in the second print, some

of the layers experienced poor inter-layer adhesion, made evident through the visual inspection of the part. Light could be seen through several layer boundaries, indicating gaps in the part. This poor adhesion is attributed to the substrate temperature not being sufficiently above the glass transition temperature [23]. In Section 3.3 it was concluded that the relationship between the geometric features of the part and failure would add a degree of complexity to the experiment, and render the 1-dimensional heat transfer model, described in Section 3.8, useless. However, the results from these prints served as motivation to further pursue this research. Figure 4.1 below depicts the two hexagon geometries. Appendix D contains more pictures of the printed geometries' definition and poor inter layer adhesion, and the layer-by-layer thermal imaging analysis of each hexagon during the entire printing process.

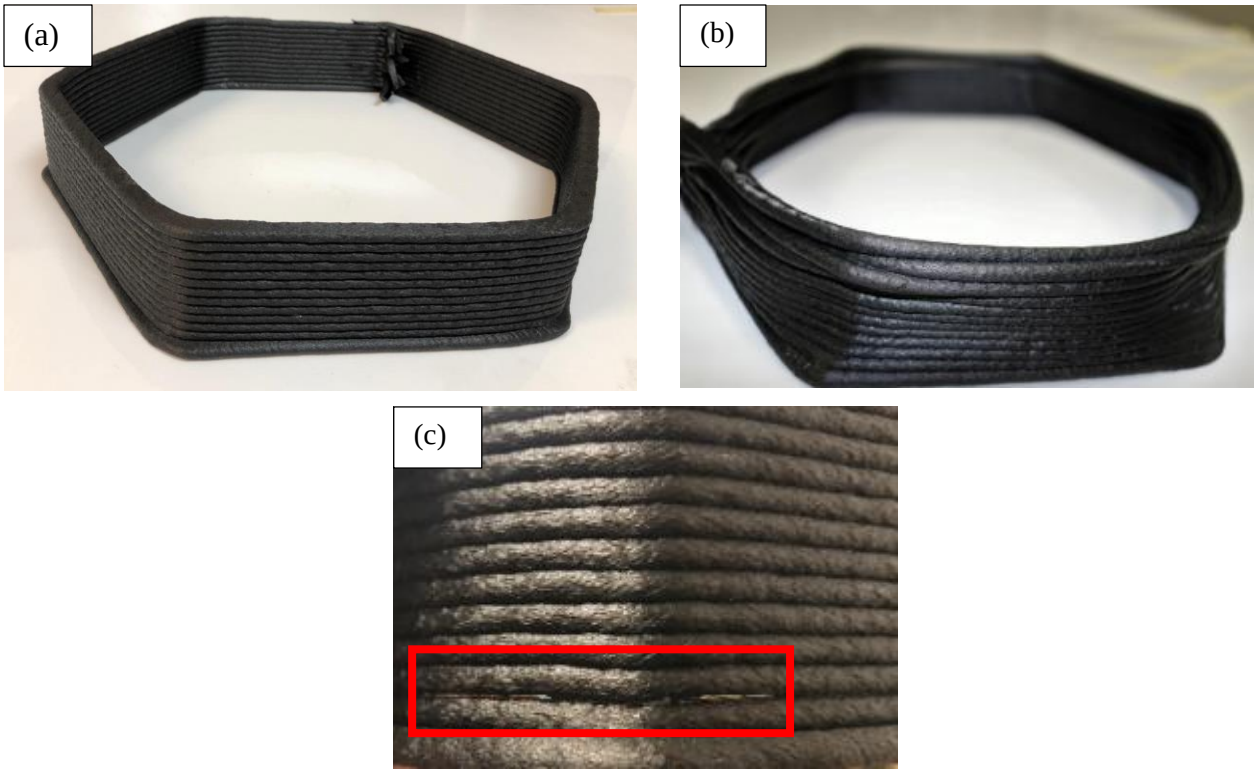

Figure 4.1 The hexagon geometries printed with the BAAM machine. Frame (a) depicts a hexagon printed with a 90 second delay between layers, while frame (b) depicts a hexagon geometry printed with no added layer time. Notice the difference in print quality where the part shown in (b) is defective. Frame (c) shows an interlayer gap (inside the red square) in the hexagon depicted in frame (a).

4.3 Single-Bead Wall in Situ Temperature Analysis and Video Analysis

The print experienced adhesion problems during the deposition of layer 7. As layer 7 was being deposited, the underlying substrate experienced compressive deformation, thus resulting in the deposited material not being directly above the substrate, but rather diagonally above it. Furthermore, as layer 9 was being deposited, layer 8 collapsed in the direction of the camera, i.e., layer 8 failed to properly adhere to the substrate when bearing the load of layer 9. The subsequent layers, while adhering to the substrate, do not conform to the desired dimensional geometry of the

part, as they are deposited on top of a deformed substrate. The final layers do not adhere to the substrate and fall to the print bed.

The temperature of the substrate just before the deposition of a new layer reaches a steady state after the deposition of the fifth layer, as can be seen in Figure 4.2 below. Although collapse and failure to adhere are seen in layer 08 and subsequent layers, plastic deformation can be seen right after the deposition of layer 05, as can be seen in Figure 4.3 below. Appendix D contains the thermal imaging analysis for each layer of this single-wall print, over the entire printing process.

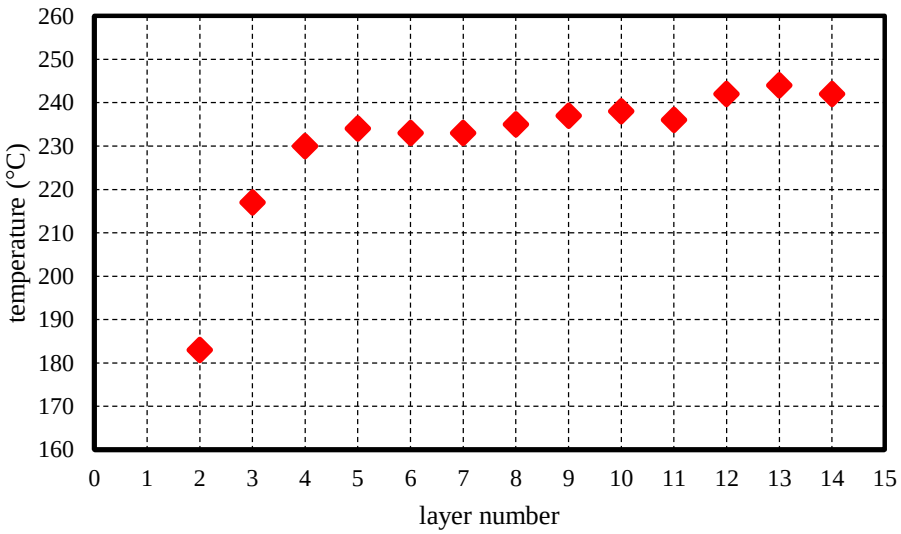

Figure 4.2 The highest recorded temperature in the substrate just before the deposition of the layer represented in the x-axis. Notice how the temperature remains above 230 °C after the deposition of the fourth layer.

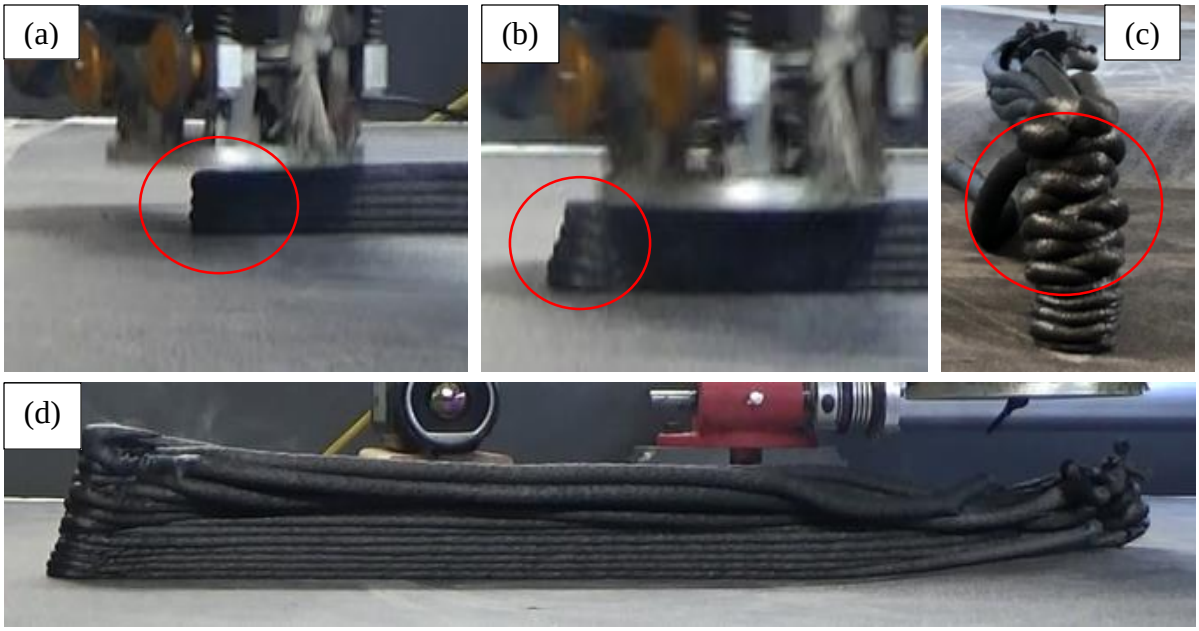

Figure 4.3 The plastic deformation of the substrate in the printing direction just after the deposition of layer 5. The first (a) frame shows layer 5 being deposited, and the second (b) frame shows the substrate right after the deposition of layer 5. Notice the comparison between the substrate inside the red circles in frames (a) and (b). The third frame (c) shows the side view of the finalized print. Notice the diagonal stacking of layers inside the red circle. Finally, the last frame (d) shows the finalized print. Notice the deformation in the top layers.

The initial failure occurs when the substrate experiences deformation due to the load applied by the extruder depositing a new layer. If the start of the print is misaligned – usually caused by leftover material at the tip of the nozzle – the underlying material will deform in conformance with this initial misalignment, and thus causing a "zig-zag" diagonal stacking deposition, as can be seen in Figure 4.3 above. Although the material is initially successfully deposited, this "zig-zag" effect causes failure to adhere to proper dimensions, i.e., a shorter part, and results in new layers eventually being deposited on mid-air as a consequence.

The deposition temperature used for this print can be seen in Table 3.1 in Section 3.1 of this document. Although the melt temperature is set at 225 °C, that is just a reference value for the operator and does act like a setpoint temperature. Accurate temperature is obtained by the melt thermocouple during printing, which for this experiment indicated a temperature of ~240 °C, as

can be seen in Figure 4.4 below. Notice the deposition temperatures remain just above 240 °C in layer 4 and subsequent layers, reaching a maximum recorded temperature just after deposition of 247 °C.

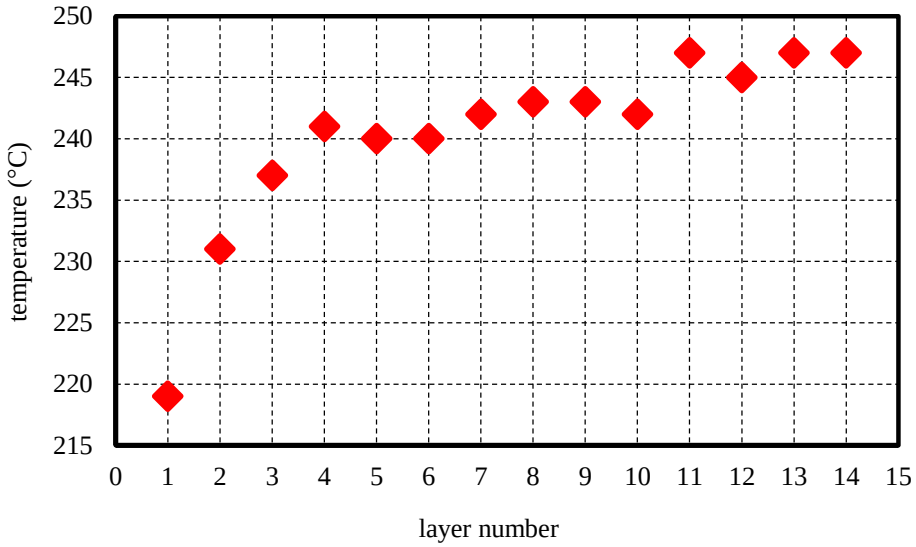

Figure 4.4 The temperature of every layer just after deposition. Notice how the deposition temperature remains above 240 °C after layer 04.

4.4 Compression Testing

Every compression curve obtained from testing followed a similar shape. However, the compression curves for the tests conducted at 90, 110, 130 and 150 °C all have an initial loading section, a linear elastic region, a plateau, and a final load bearing region, albeit at different displacement and loading conditions. The compressive behavior where the plateau is present is analogous to the compression behavior of foam and porous materials [38]. BAAM-printed parts, in addition to possessing porosity between the deposited layers in the substrate, also have porosity in the cross-section of a printed bead – as will be discussed in the following section [24, 27]. Figure 4.5 below shows the average compression curves for every specimen set at each temperature.

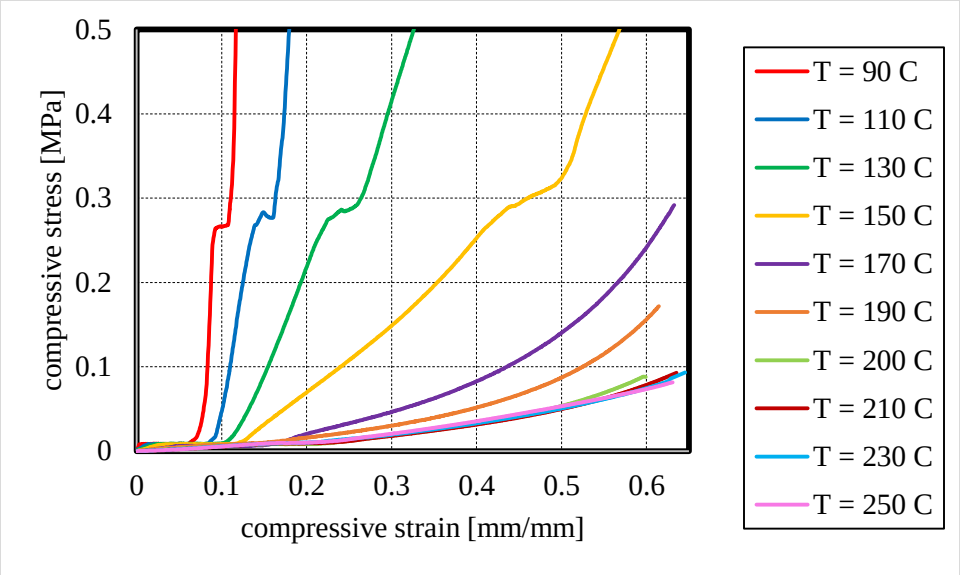

Figure 4.5 The compressive behavior of the specimens tested at ten different temperatures. The plateau region is only present in the curves at 90, 110, 130 and 150 °C. Notice that the compressive behavior remains constant in curves where the temperature is 200 °C or higher.

In the compression curves, an inverse relationship was found between the temperature of the specimen and the load withstood just before reaching a strain level of approximately 60 percent. Additionally, it is noticed that the tests conducted at a temperature of 170 °C and above, do not possess a plateau region. Appendix D contains the individual sets of compression curves from each temperature. The average loads at which a strain level of 15, 30, and 60 percent (chosen as arbitrary points along the x-axis) were reached for every temperature can be seen in Table 4.1 below.

Table 4. 2 The average compressive load and compressive stress to reach strain levels of 15, 30 and 60 percent at every temperature level. Notice the declining trend in load as the temperature increases.

temperature [°C]	compressive load [N] at ε = 15%	compressive stress [MPa] at ε = 15%	compressive load [N] at ε = 30%	compressive stress [MPa] at ε = 30%	compressive load [N] at ε = 60%	compressive stress [MPa] at ε = 60%
90	453.61	4.45	3017.89	29.61	6121.43	60.06
110	28.81	0.28	257.88	2.52	1678.57	16.43
130	9.08	0.09	42.11	0.42	193.95	1.91
150	3.20	0.03	15.16	0.15	59.82	0.59
170	0.71	0.01	4.73	0.05	24.76	0.24
190	1.04	0.01	3.23	0.03	16.81	0.16
200	0.81	0.01	1.86	0.02	9.09	0.09
210	0.86	0.01	1.86	0.02	8.07	0.08
230	0.88	0.01	1.99	0.02	7.63	0.07

250	0.89	0.01	2.09	0.02	7.53	0.07

At a temperature of 210 °C and above, the material compressive behavior is virtually the same. It is significant to notice that, going back to the single-wall print, 210 °C is the temperature at which deformation was first observed in the printing process, right after deposition of layer 04. The observed compressive behavior remained constant when considering the compressive stress-strain behavior and the compressive load-displacement behavior. A graph displaying the compressive load against the compressive displacement can be found in Appendix D.

4.5 Porosity

Porosity was observed in the tested samples. As mentioned in the previous section, some of the compression curves obtained experimentally have a plateau region, resembling the compressive behavior of a porous material [38]. Figure 4.6 below shows the optical imaging pictures obtained from the cross-section of four specimens, compressed at a temperature of 130 °C to 0.2 mm, 0.7 mm, 1.0 mm, and 1.2 mm. Porosity can be visually appreciated in Figure 4.6 below. Figure 4.7 below shows the relative porosity content in every specimen.

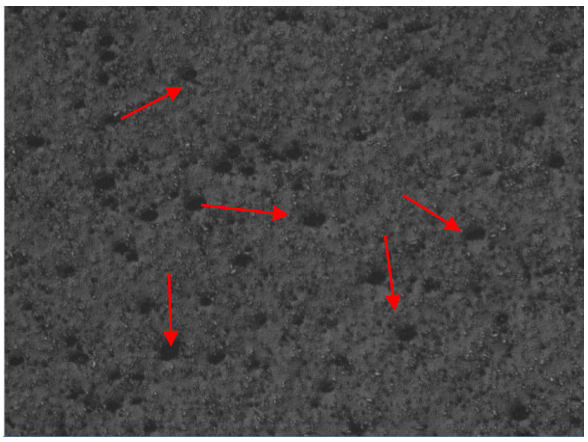

Initial loading (Δx = 0.2 mm)

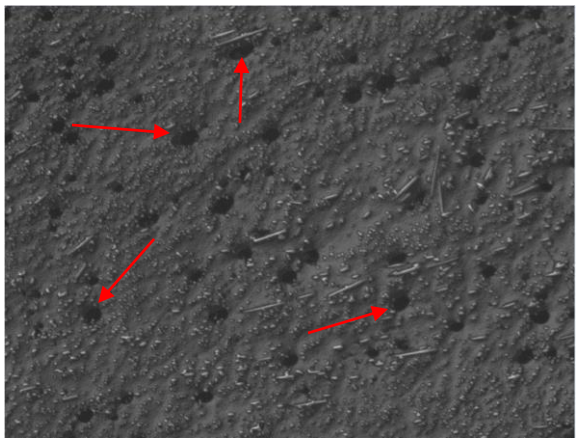

linear elasticity (Δx = 0.7 mm)

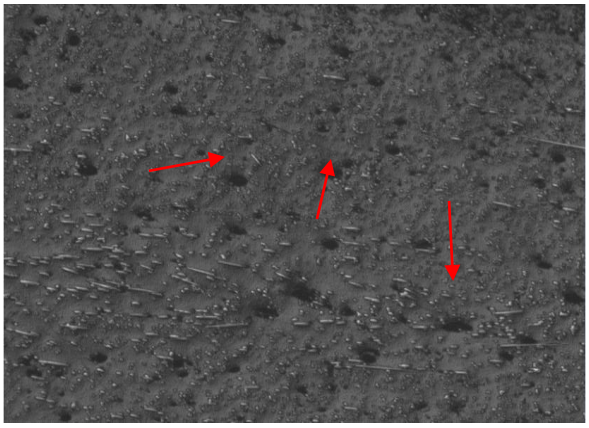

plateau (Δx = 1.0 mm)

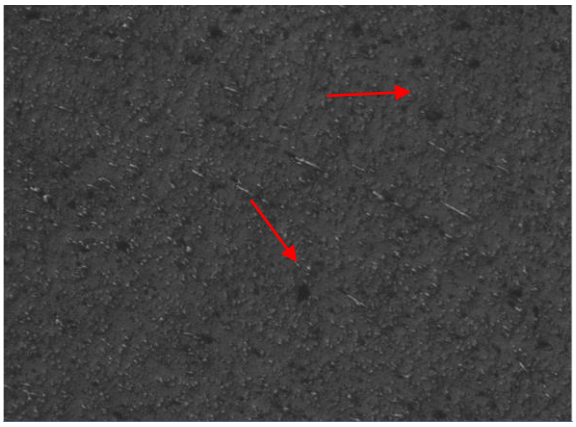

densification (Δx = 1.2 mm)

Figure 4.6 The cross-section optical imaging analysis (5x magnification) of the ABS-20CF BAAM printed parts compressed at four displacement levels at 130 °C, each corresponding to a different region in the compression curve seen in Figure 5. The red arrows point at the pores in the cross-section images. As predicted, the pore size and quantity decrease as the compression displacement increases, in particular after the plateau region. This compressive behavior is distinctly observed in porous materials.

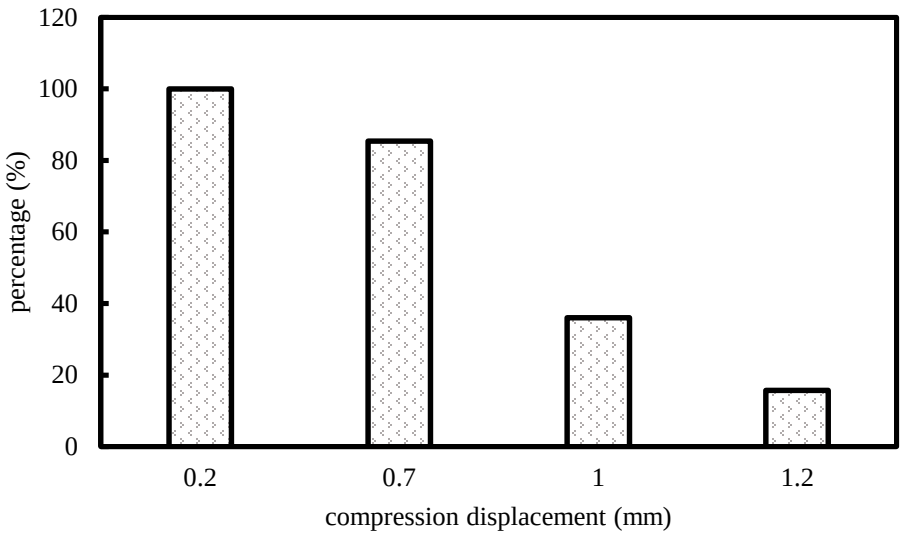

Figure 4.7 The porosity analysis as a percentage in every sample. One-hundred percent is used as a comparative reference tool to compare the specimen with the most porosity to the rest of the samples. Notice that the porosity decreases by over 80 percent from the piece with the compressive displacement of 0.2 mm to the one with 1.2 mm.

4.6 Rheological Properties

Figure 4.8 below shows the storage modulus and the tan delta obtained from the rheological testing at nine different temperatures ranging from 160 to 230 °C. Notice the tan delta curve, in conjunction with the storage modulus, indicate the transition between the rubbery plateau – where the material behaves like an elastic rubber - and the rubbery flow region – where the material acts more similarly to an easily deformable liquid. As can be seen in Figure 4.8 below, a temperature of 200 °C in ABS-20CF represents the onset temperature at which the material transitions from the rubbery plateau region into the rubbery flow region. This transition is noticed in the tan(δ) curve where the slope of the curve becomes positive after the plateau, and in the storage modulus curve where the modulus steadily declines. This transition represents a change in the viscoelastic behavior of the material, from being able to withstand loads while retaining its shape, to

experiencing deformation as a result of compressing loading – conforming to the previously mentioned compressive deformation behavior.

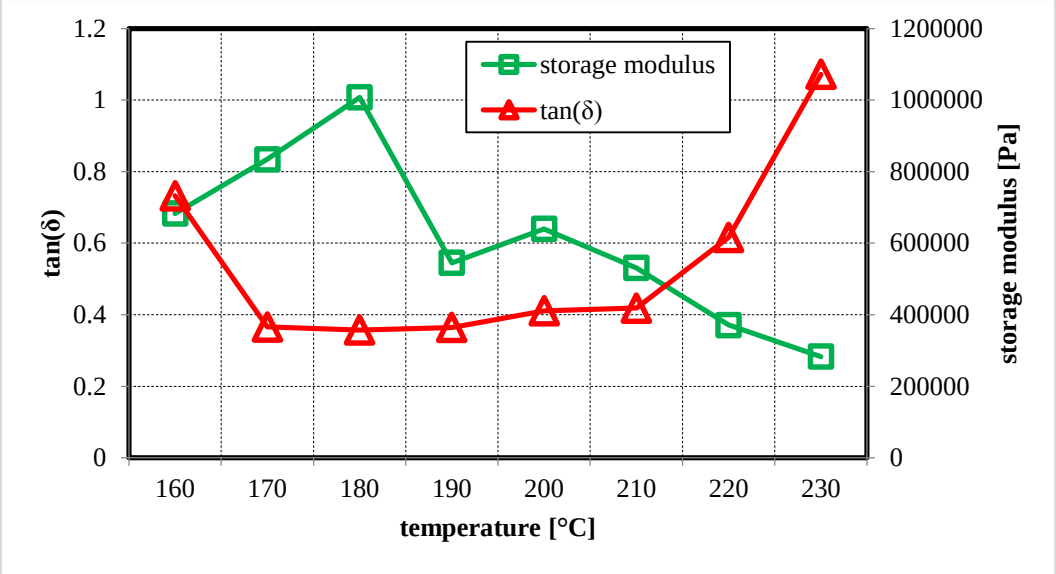

Figure 4.8 The storage modulus and tan(δ) analysis of ABS-20CF pellets at a frequency of 628 rad/s. Notice that 200 C is the onset temperature at which the transition occurs between the rubbery plateau and the rubbery flow region. Lines are intended to guide the eyes.

Figure 4.9 below shows the tan(δ) graph of the eight sets of experiments conducted at temperatures of 160 to 230 °C, over the frequency range of 0.1 rad/s to 628 rad/s. Notice that the curves at temperatures of 190 °C and below exhibit a negative slope trend. This trend changes in the curve at 200 °C, where the slope flattens. In the curves at a temperature of 210 °C and above, the slope has an initial positive slope trend, meaning that the loss modulus dominates over the elastic modulus and as such, the part tends to exhibit more viscous properties. It can be noticed the part exhibits a more viscous behavior with increasing temperature at angular frequencies higher than 10 rad/s. During a BAAM print, the material experiences shear rates of 30-40 Hz (189-251 rad/s) in the barrel, and 100 Hz (628 rad/s) at the exit of the nozzle [47]. The high value in the tan(δ) at frequencies close to 628 rad/s represents the transition between the leather and rubber plateau viscoelastic regions of the material [29].

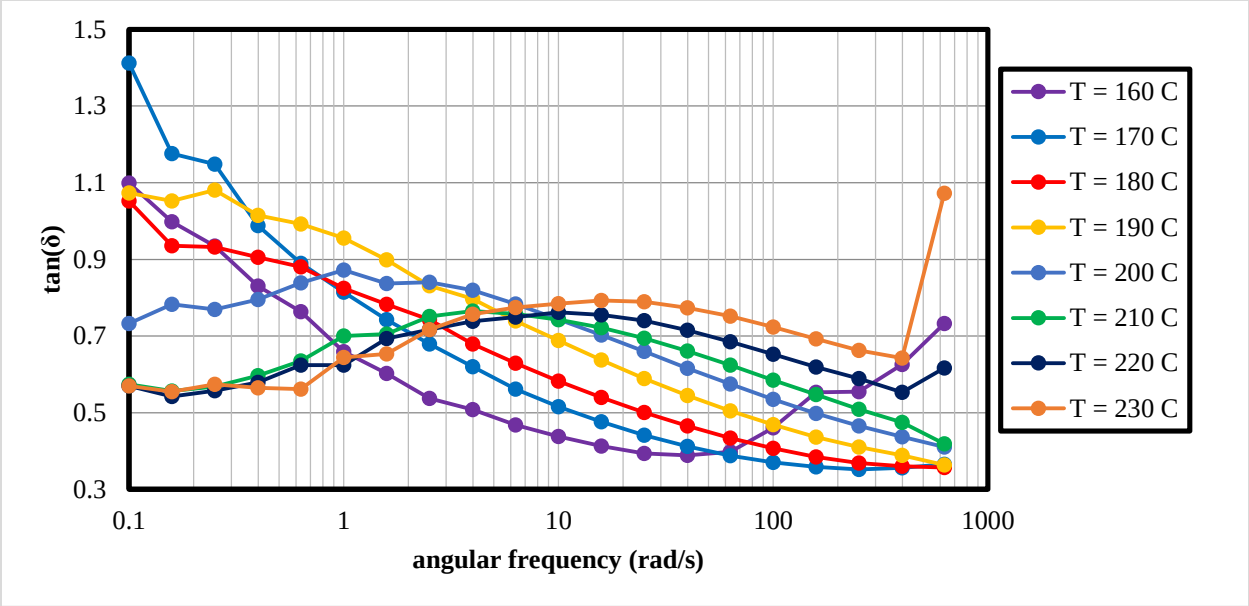

Figure 4.9. The tan(δ) curve of ABS-20CF, obtained through dynamic melt rheology testing. Notice the shift in slope trend that occurs between the temperatures of 190 °C and 210 °C.

4.7 Final Prints

Using the model developed by Compton *et al*. [23], a layer time was calculated to regulate the substrate temperature. Figure 4.10 below shows the highest temperature recorded in the substrate just prior to the deposition of a new layer, for both prints. In the print where the substrate temperature was controlled to remain under 200 °C, twenty-one layers were successfully printed without any deformation that resulted in collapse, as can be seen in Figure 4.10 below. Some deformation is seen at the start of almost every printed layer (attributed to residual material in the tip of the nozzle). However, the layer path is eventually corrected, and the layer is successfully deposited. The success of the print is attributed to the substrate presenting a more elastic, rather than viscous behavior, as well as enough compressive strength, making it resistant to plastic deformation and able to hold its shape.

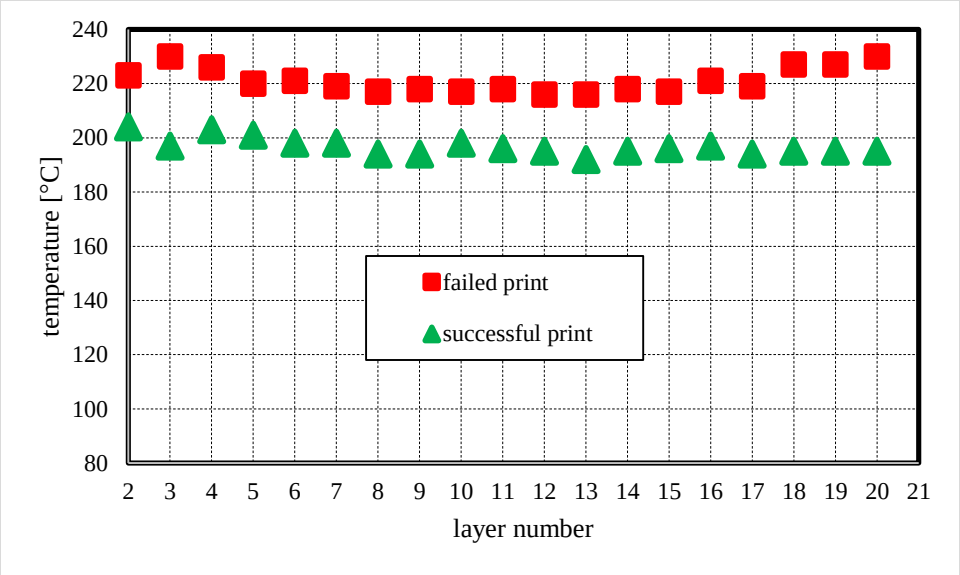

Figure 4.10 The temperature of the substrate just prior to the deposition of a new layer in the final two prints. Notice the successful print substrate temperature remained at ~200 °C, while the failed print remained at ~220 °C.

In the print where the substrate temperature was controlled to be just under 220 °C, a deformation that resulted in the overall collapse was observed. Twenty layers were printed in this part. Deformation was observed in layer 05, which experienced deformation during the deposition of layer 06, resulting in diagonal, or "zig-zag," stacking. Eventually, layer 10 and subsequent layers were deposited into mid-air and thus failed to adhere properly to the substrate, resulting in overall collapse and failure, as can be seen in Figure 4.11 below.

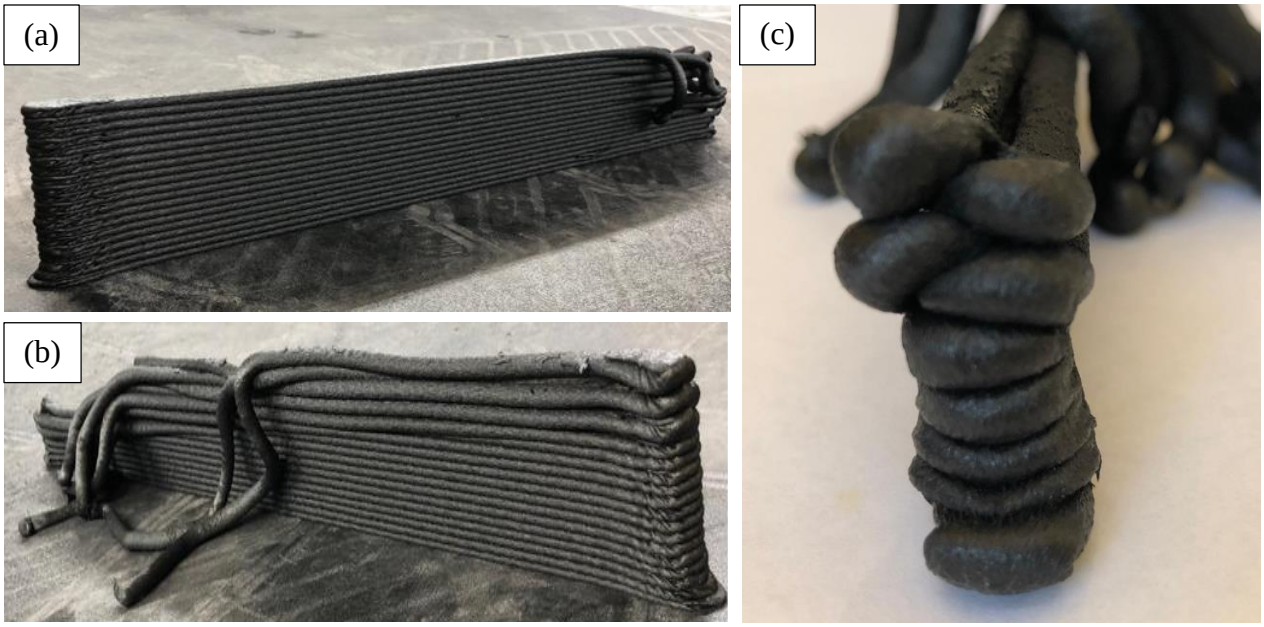

Figure 4.11 The final prints with added layer time. In the first frame (a), the temperature was controlled to be just below 200 °C prior to the deposition of a new layer. In frames (b) and (c), the temperature was controlled to be just below 220 °C prior to the deposition of a new layer. Notice the deformation comparison between the two temperatures. Also, notice the "zig-zag" effect that leads to overall collapse in frame (c).

Chapter 5

Conclusion

5.1 Concluding Remarks

In large area pellet extrusion additive manufacturing, the temperature of the substrate just before the deposition of a new subsequent layer affects the overall structure of the part. Deformation and layer adhesion failure occur if the substrate temperature is above a certain threshold just before deposition of a new layer. Currently, Big Area Additive Manufacturing (BAAM) machine users mitigate this problem by trial and error, which is costly and may result in decreased mechanical properties, monetary losses and time inefficiencies.

Through in situ thermal imaging, the range of temperatures at which unwanted deformation occurs during the printing of an ABS-20CF BAAM single bead thin wall was identified. Compression tests were then performed to understand the compressive behavior at this identified range of temperatures. A plateau region was detected in the compression curves at temperatures of 170 °C and below – a behavior attributed to the porosity found through optical imaging in the cross section of a printed bead. As expected, the compressive strength of a part decreases with temperature; however, at temperatures of 200 °C and above, the compressive strength remains constant. From the thermography of the three single-bead thin wall prints, in conjunction with the compression testing, it was concluded that, starting at a temperature of 200 °C, the underlying substrate cannot withstand the compressive loads applied by the extruder depositing a newly added layer, and the tamper mechanism, without experiencing significant deformation.

To corroborate this, the rheological testing concluded that 200 °C is the temperature which onsets the transition between the region where an elastic behavior is more prevalent to the region where a viscous behavior is more dominant. It was concluded that if the substrate is above a

temperature of 200 °C at the time a new layer is deposited, the substrate will experience compressive deformation. Above this temperature threshold, the substrate experiences deformation in such a way that a new layer is deposited diagonally above it, instead of directly above – attributed to compressive deformation and a tendency of the material to flow. This diagonal deposition results in a shorter part. Subsequent depositions build on this initial failure, resulting in a cascade of deformation (termed "zig-zag") in which every subsequent deposition brings the part further away from its intended dimensions, until eventually material is deposited in mid-air.

5.2 Recommendations for Future Work

Although this paper identified the upper temperature bound at which printing can be performed without compromising geometrical fidelity (i.e. presenting sagging or drooping), the temperature at which inter-layer adhesion is optimized remains unknown and is therefore recommended as a subject of future research. In addition, although the scope of this work was solely focused on ABS-20CF, it can be extrapolated to encompass a broader range of BAAM-compatible materials.

Although the temperature presented in this research prevents unwanted deformation at high temperatures, the effect of part geometry is not taken into consideration in this research. The compressive and rheological results presented in this paper only account for a single-bead vertical wall feature. Similarly, although only a tool to assist with temperature control, the use of a thermal model to predict the substrate's temperature only accounts for 1-dimensional heat transfer. As such, the temperature threshold suggested in this paper is a guideline for single-bead vertical walls only. Further work would encompass a relationship between multiple complex geometries, temperature and deformation. As such, the purpose of this work is to be a stepping stone towards

the optimization of BAAM printing parameters to improve geometric fidelity and inter-layer strength.

References

[1] ASTM International, “F2792-12a: Standard Terminology for Additive Manufacturing Technologies,” *Annu. B. ASTM Stand.*, 2012.

[2] A. Roschli *et al.*, “Designing for Big Area Additive Manufacturing,” *Addit. Manuf.*, vol. 25, no. September 2018, pp. 275–285, 2019.

[3] V. K. Christine Ajinjeru Xun Chen John Lindahl Zeke Sudbury Ahmed Hassen Vlastimil Kunc Brian Post Lonnie Love Chad Duty, “The Influence of Rheology on Melt Processing Conditions of Amorphous Thermoplastics for Big Area Additive Manufacturing (BAAM),” *Solid Free. Fabr. Symp.*, p. 8, 2016.

[4] I. Gibson, D. W. Rosen, and B. Strucker, *Additive Manufacturing Technologies: 3D Printing, Rapid Prototyping, and Direct Digital Manufacturing*, Second. New York: Springer, 2010.

[5] E. M. Sachs, M. J. Cima, and J. Cornie, “Three Dimensional Printing: Rapid Tooling and Prototypes Directly from CAD Representation,” in *Solid Freeform Fabrication Symposium*, 1990, pp. 27–47.

[6] S. Meteyer, X. Xu, N. Perry, and Y. F. Zhao, “Energy and material flow analysis of binder-jetting additive manufacturing processes,” *Procedia CIRP*, vol. 15, pp. 19–25, 2014.

[7] P. K. Gokuldoss, S. Kolla, and J. Eckert, “Additive manufacturing processes: Selective laser melting, electron beam melting and binder jetting-selection guidelines,” *Materials (Basel).*, vol. 10, no. 6, 2017.

[8] A. J. Pinkerton, “Lasers in additive manufacturing,” *Opt. Laser Technol.*, vol. 78, pp. 25–32, 2016.

[9] H. Almeida and M. Correla, “Sustainable Impact Evaluation of Support Structures in the Production of Extrusion-Based Parts,” in *Handbook of Sustainability in Additive Manufacturing*, vol. 1, Singapore: Springer, 2016, pp. 7–30.

[10] J. C. Heigel, P. Michaleris, and E. W. Reutzel, “Thermo-mechanical model development and validation of directed energy deposition additive manufacturing of Ti-6Al-4V,” *Addit. Manuf.*, vol. 5, pp. 9–19, 2015.

[11] B. N. Turner and S. A. Gold, “A review of melt extrusion additive manufacturing processes: II. Materials, dimensional accuracy, and surface roughness,” *Rapid Prototyp. J.*, vol. 21, no. 3, pp. 250–261, 2015.

[12] P. Blake, E. Fodran, M. Koch, U. Menon, and B. Priedeman, “FDM of ABS Patterns for Investment Casting,” in *1997 International Solid Freeform Fabrication Symposium*, pp. 195–202.

[13] Loughborough University Additive Manufacturing Research Group, “About Additive Manufacturing.” [Online]. Available: https://www.lboro.ac.uk/research/amrg/about/.

[14] F. Gao and A. A. Sonin, “The Physics of Digital Microfabrication with Molten

Microdrops," in *1993 International Solid Freeform Fabrication Symposium*, 1993, pp. 237–244.

[15] W. E. King, A. T. Anderson, R. M. Ferencz, N. E. Hodge, and C. Kamath, "Laser Powder Bed Fusion Additive Manufacturing of Metals; Physics , Computational , and Materials Challenges," *Appl. Phys. Rev.*, vol. 2, 2015.

[16] H. Gong, K. Rafi, H. Gu, T. Starr, and B. Stucker, "Analysis of defect generation in Ti-6Al-4V parts made using powder bed fusion additive manufacturing processes," *Addit. Manuf.*, vol. 1, pp. 87–98, 2014.

[17] S. A. Khairallah, A. T. Anderson, A. M. Rubenchik, and W. E. King, "Laser powder-bed fusion additive manufacturing: Physics of complex melt flow and formation mechanisms of pores, spatter, and denudation zones," *Addit. Manuf. Handb. Prod. Dev. Def. Ind.*, vol. 108, pp. 613–628, 2017.

[18] D. F. Walczyk and D. Hardt, "Rapid Tooling for Sheet Metal Forming using Profiled Edge Laminations - Design Principles and Demonstration," *J. Manuf. Sci. Eng.*, vol. 4, 1998.

[19] T. Nakagawa, M. Kunieda, and S. D. Liu, "Laser Cut Sheet Laminated Forming Dies by Diffusion Bonding," in *Proceedings of the Twenty-Fifth International Machine and Research Conference*, 1985.

[20] N. A. Chartrain, C. B. Williams, and A. R. Whittington, "A review on fabricating tissue scaffolds using vat photopolymerization," *Acta Biomater.*, vol. 74, pp. 90–111, 2018.

[21] G. I. Peterson *et al.*, "Production of Materials with Spatially-Controlled Cross-Link Density via Vat Photopolymerization," *ACS Appl. Mater. Interfaces*, vol. 8, no. 42, pp. 29037–29042, 2016.

[22] L. Li, "Analysis and fabrication of FDM Prototypes with locally controlled properties," 2002.

[23] B. G. Compton, B. K. Post, C. E. Duty, L. Love, and V. Kunc, "Thermal analysis of additive manufacturing of large-scale thermoplastic polymer composites," *Addit. Manuf.*, vol. 17, pp. 77–86, 2017.

[24] C. E. Duty *et al.*, "Structure and mechanical behavior of Big Area Additive Manufacturing (BAAM) materials," *Rapid Prototyp. J.*, vol. 23, no. 1, pp. 181–189, 2017.

[25] S. Crump, "Apparatus and method for creating three-dimensional objects," 5,121,329, 1992.

[26] Stratasys Ltd., "Our Materials." [Online]. Available: https://www.stratasys.com/materials/search.

[27] E. Macdonald *et al.*, "Spatial frequency analysis for improved quality in Big Area Additive Manufacturing (BAAM)," in *Proceedings of the ASME 2017 International Mechanical Engineering Congress and Exposition*, 2017, pp. 1–5.

[28] Cincinnati, "2016 BAAM Fact Sheet," 2016.

[29] J. D. Menczel and R. B. Prime, *Thermal Analysis of Polymers: Fundamentals and Applications*. Wiley, 2009.

[30] R. M. Jones, *Mechanics of Composite Materials*, 2nd ed. New York: Taylor & Francis, 1999.

[31] P. Parandoush and D. Lin, "A review on additive manufacturing of polymer-fiber composites," *Compos. Struct.*, vol. 182, pp. 36–53, 2017.

[32] S. Yang, J. R. Castilleja, E. V. Barrera, and K. Lozano, "Thermal analysis of an acrylonitrile-butadiene-styrene/SWNT composite," *Polym. Degrad. Stab.*, vol. 83, no. 3, pp. 383–388, 2004.

[33] B. Brenken, E. Barocio, A. Favaloro, V. Kunc, and R. B. Pipes, "Fused filament fabrication of fiber-reinforced polymers: A review," *Addit. Manuf.*, vol. 21, no. October 2017, pp. 1–16, 2018.

[34] L. J. Love *et al.*, "The importance of carbon fiber to polymer additive manufacturing," *J. Mater. Res.*, vol. 29, no. 17, pp. 1893–1898, 2014.

[35] T. Hofstätter, D. B. Pedersen, G. Tosello, and H. N. Hansen, "Applications of Fiber-Reinforced Polymers in Additive Manufacturing," *Procedia CIRP*, vol. 66, pp. 312–316, 2017.

[36] E. A. Collins, J. Bares, and F. W. Billmeyer, *Experiments in Polymer Science*. New York: Wiley-Interscience, 1973.

[37] ASTM International, "E9-09: Standard Test Methods of Testing," *Annu. B. ASTM Stand.*, 2018.

[38] M. S. Rajput, M. Burman, J. Köll, and S. Hallström, "Compression of structural foam materials – Experimental and numerical assessment of test procedure and specimen size effects," *J. Sandw. Struct. Mater.*, vol. 21, no. 1, pp. 260–288, 2019.

[39] B. Budiansky and N. Fleck, "Compressive Failure of Fibre Composites," *J. Mech. Phys. Solids*, vol. 41, no. I, pp. 183–211, 1993.

[40] D. Adams *et al.*, "An Evaluation of Composite Material Compression Test Methods," *J. Compos. Technol. Res.*, vol. 11, no. 2, p. 41, 2010.

[41] V. T. Marla, R. L. Shambaugh, and D. V. Papavassiliou, "Use of an infrared camera for accurate determination of the temperature of polymer filaments," *Ind. Eng. Chem. Res.*, vol. 46, no. 1, pp. 336–344, 2007.

[42] J. Welty, G. L. Rorrer, and D. G. Foster, *Fundamentals of Momentum, Heat and Mass Transfer*, 6th ed. New York: Wiley, 2014.

[43] J. Montesano, Z. Fawaz, and H. Bougherara, "Use of infrared thermography to investigate the fatigue behavior of a carbon fiber reinforced polymer composite," *Compos. Struct.*, vol. 97, pp. 76–83, 2013.

[44] R. Steinberger, "Infrared thermographic techniques for non-destructive damage characterization of carbon fibre reinforced polymers during tensile fatigue testing," *Int. J.*

Fatigue, vol. 28, pp. 1340–1347, 2006.

[45] ASTM International, "D695-15: Standard Test Method for Compressive Properties of Rigid Plastics," *Annu. B. ASTM Stand.*, 2015.

[46] ASTM International, "D4440-15: Dynamic Mechanical Properties Melt Rheology," *Annu. B. ASTM Stand.*, pp. 1–5, 2015.

[47] C. Ajinjeru *et al.*, "Rheological evaluation of high temperature polymers to identify successful extrusion parameters," *Proc. 27th Annu. Int. Solid Free. Fabr. Symp. Addit. Manuf. Conf.*, pp. 485–494, 2017.

Appendix A

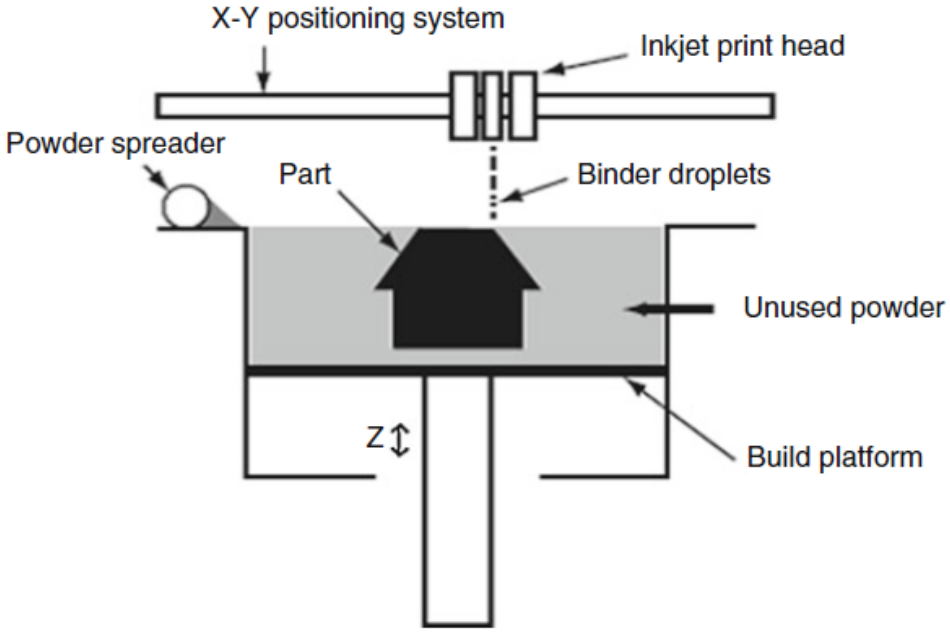

Figure A.1 An illustration of the binder jetting process [4].

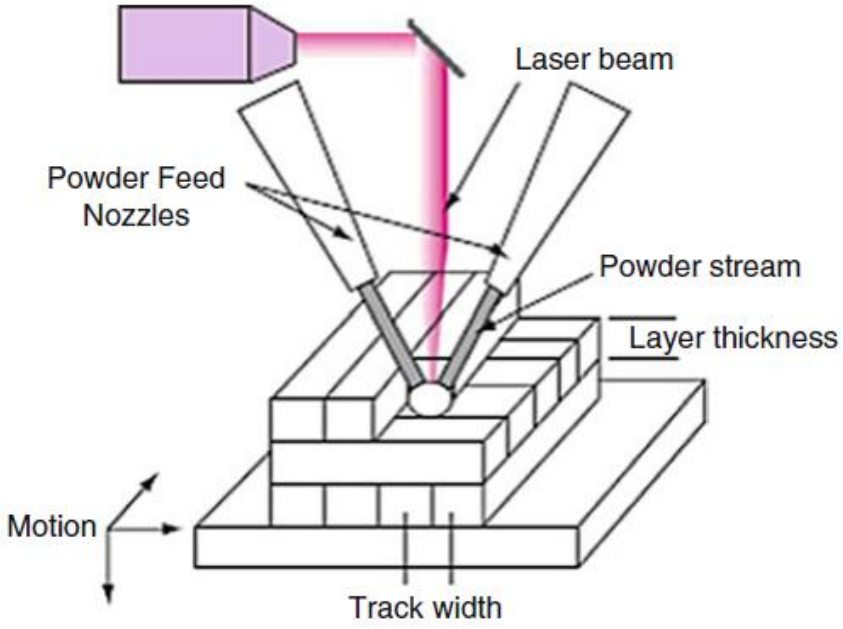

Figure A.2 An illustration of the directed energy deposition process [4].

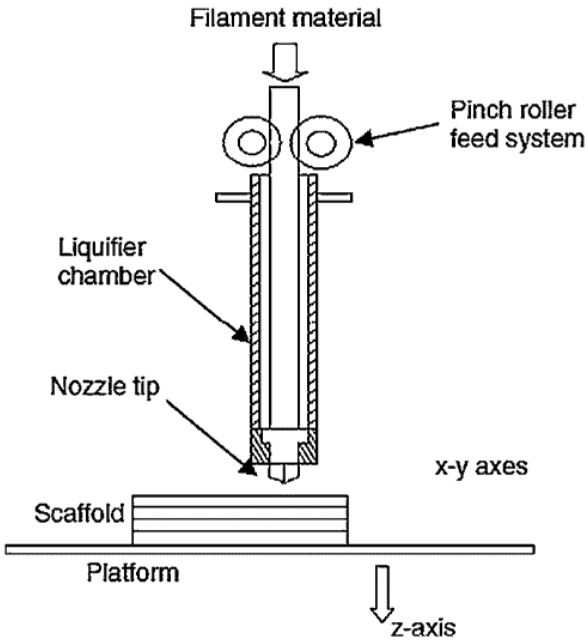

Figure A.3 An illustration of the material extrusion process, in particular, a Fused Filament Fabrication system [4].

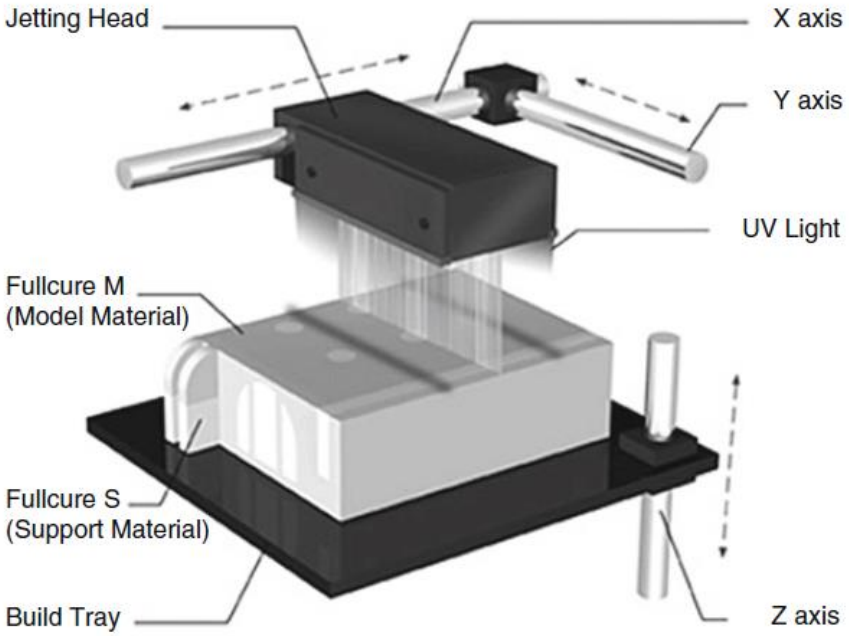

Figure A.4 An illustration of the material jetting process, in particular, the Stratasys Polyjet [4].

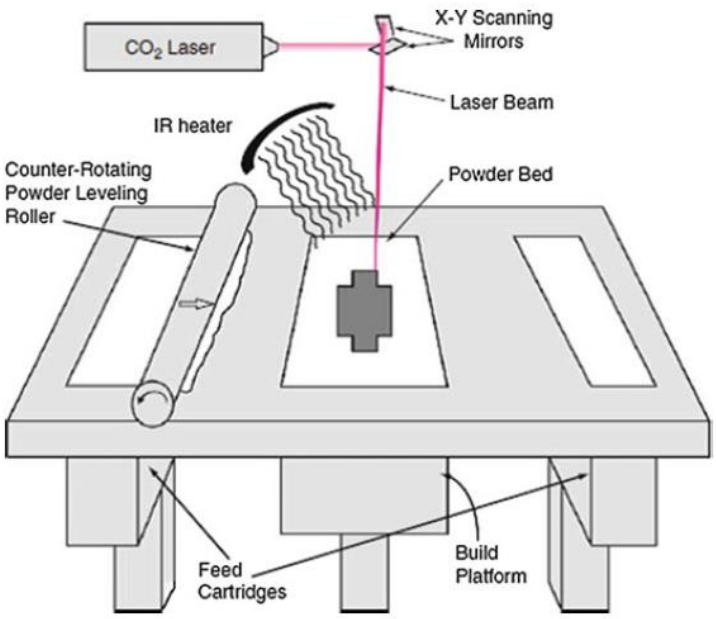

Figure A.5 An illustration of the powder bed fusion process, specifically, the Selective Laser Sintering technology [4].

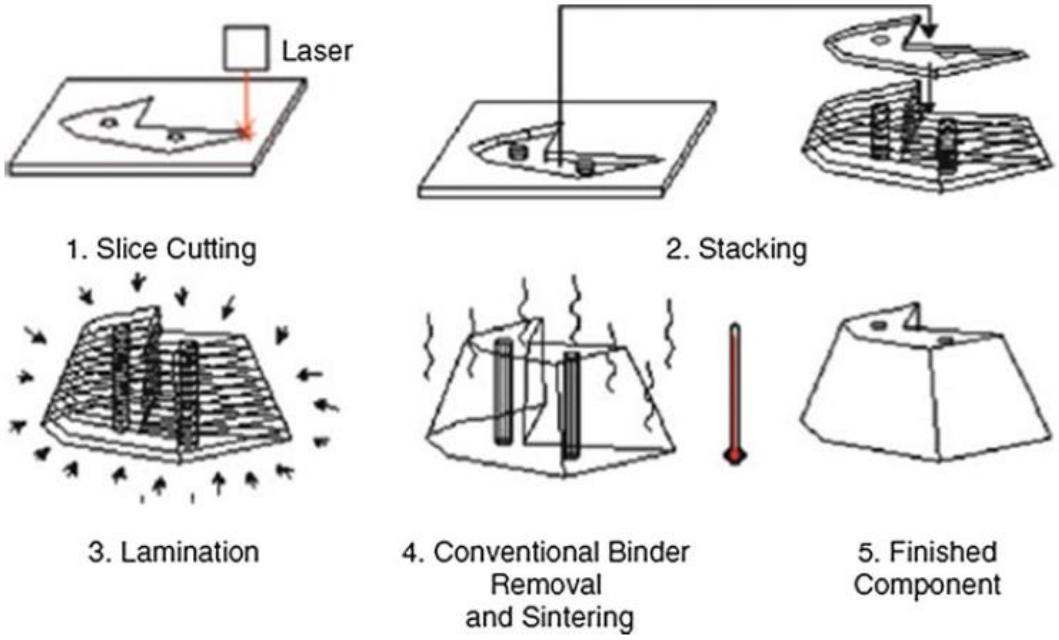

Figure A.6 An illustration of the sheet lamination process, specifically, the CAM-LEM technology [4].

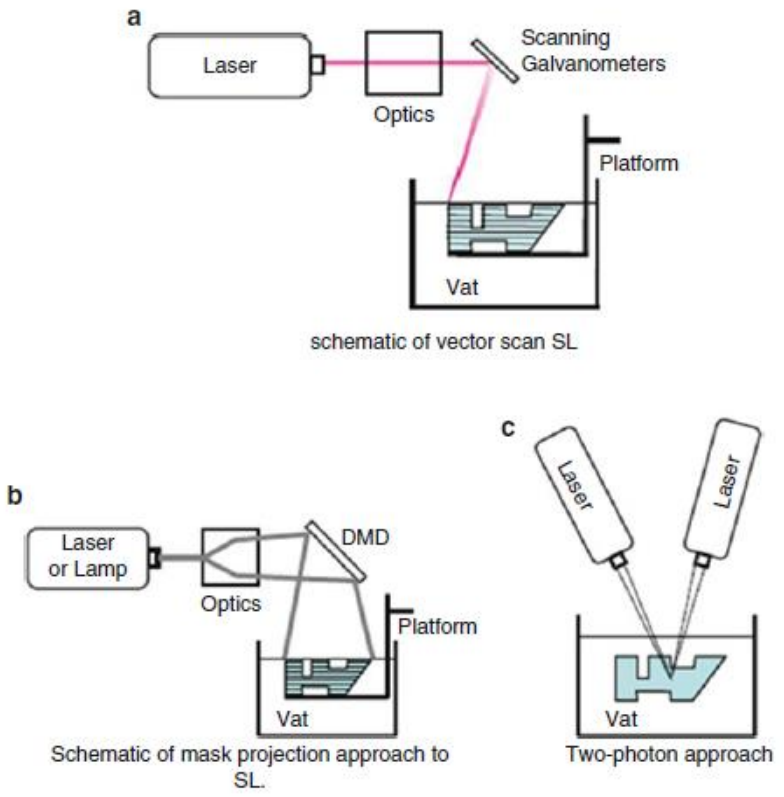

Figure A.7 An illustration of three approaches to the vat photopolymerization process [4].

Appendix B

Figure B.1 UTEP's BAAM thermoplastic extruding machine.

Figure B.2 The compressor used with the BAAM machine, used for pressuring the material feeder system.

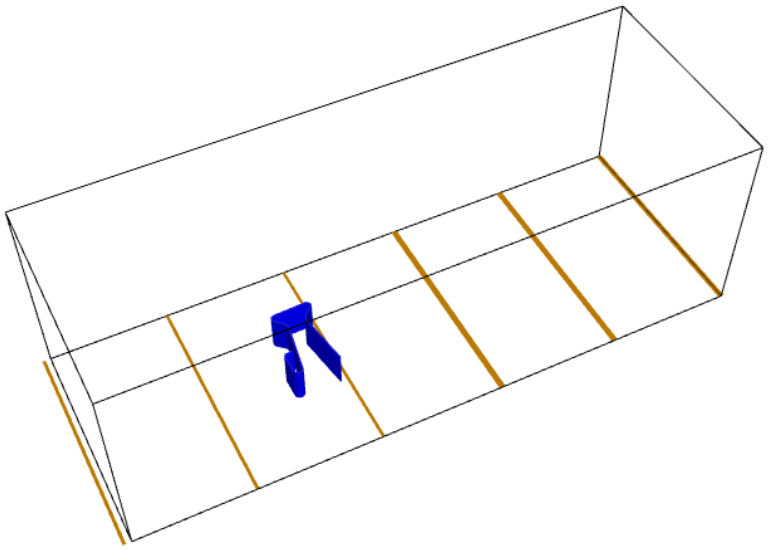

Figure B.3 A screenshot of the slicing software developed by Oak Ridge National Laboratories, with an STL model of a stool ready to be sliced.

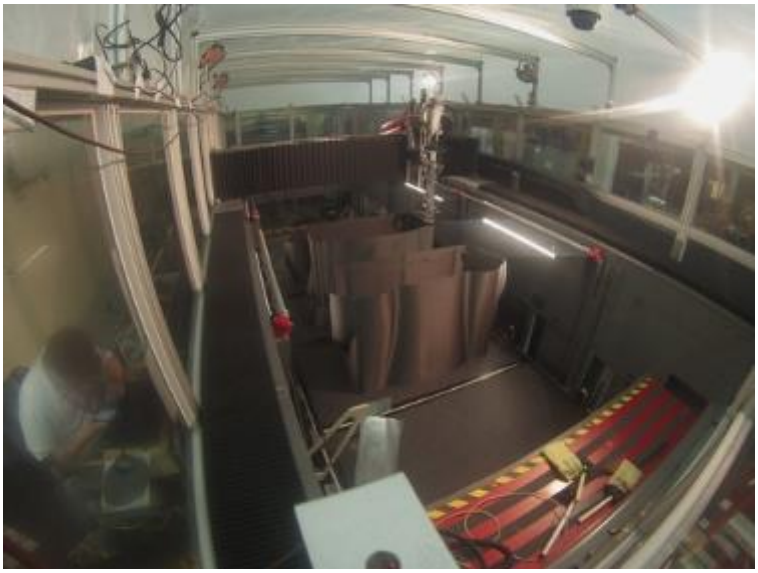

Figure B.4 The printing of a full size car with the BAAM machine, showcasing the machine's capabilities [28].

Figure B.5 The BAAM user interface, displaying the axial controls and system settings.

Appendix C

Table C.1 The dimensions of the compression test specimens

temperature [°C]	sample number	width [mm]	length [mm]	height [mm]
90	1	9.906	10.211	3.912
	2	9.887	10.192	3.937
	3	10.013	10.154	3.918
	4	10.116	10.217	3.962
	5	10.039	10.23	3.956
110	1	9.982	10.236	3.943
	2	10.077	10.255	3.956
	3	10.103	10.141	3.95
	4	10.046	10.135	4.007
	5	9.97	10.122	3.95
130	1	9.995	10.008	3.969
	2	10.046	10.135	3.943
	3	9.919	10.065	3.937
	4	9.982	10.249	3.937
	5	10.103	10.141	3.95
150	1	9.95	10.204	3.988
	2	9.944	10.243	3.962
	3	10.09	10.033	3.969
	4	10.084	10.192	4
	5	10.039	10.16	3.918
170	1	9.95	10.185	4.001
	2	10.097	10.217	3.918
	3	9.982	10.211	3.975
	4	9.919	10.23	3.924
	5	10.01	10.173	3.959
190	1	9.36	11.811	4.369
	2	9.398	11.773	4.343
	3	8.915	11.824	4.47
	4	8.884	11.773	4.394
	5	8.941	11.741	4.42
200	1	8.776	11.792	4.47
	2	8.75	11.659	4.521
	3	8.826	11.728	4.521
	4	8.75	11.595	4.585
	5	8.788	11.57	4.496
210	1	8.585	11.792	4.293
	2	8.941	11.748	4.172
	3	8.738	11.709	4.42
	4	8.522	11.722	4.572
	5	8.909	11.836	4.159
230	1	8.611	11.462	4.216
	2	8.687	11.849	4.464
	3	9.055	11.735	4.356
	4	8.687	11.735	4.445
	5	8.68	11.836	4.42

temperature [°C]	sample number	width [mm]	length [mm]	height [mm]
250	1	8.636	11.786	4.343
	2	8.827	11.544	4.343
	3	8.534	11.684	4.134
	4	8.865	11.633	4.14
	5	8.992	11.659	4.483

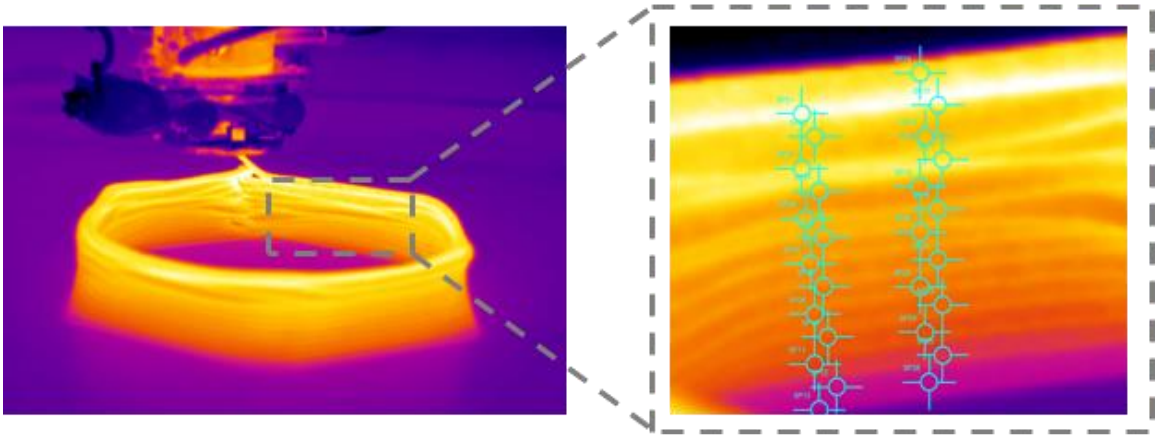

Figure C.1 A snapshot of the thermal imaging analysis of the geometry with no added time between layer depositions. The left frame shows the complete geometry, and the right frame shows a close-up of the hexagon wall, where thermal measurements were collected.

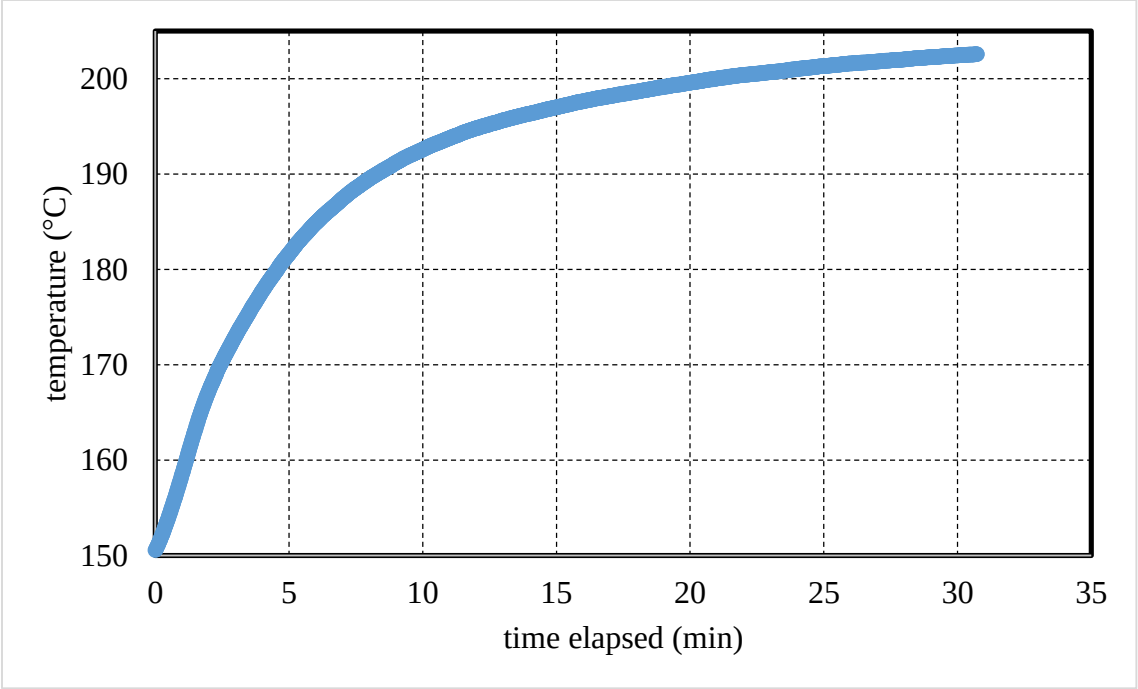

Figure C.2 The thermocouple readings as the sample was heated to a temperature of 200 °C for the emissivity calculations.

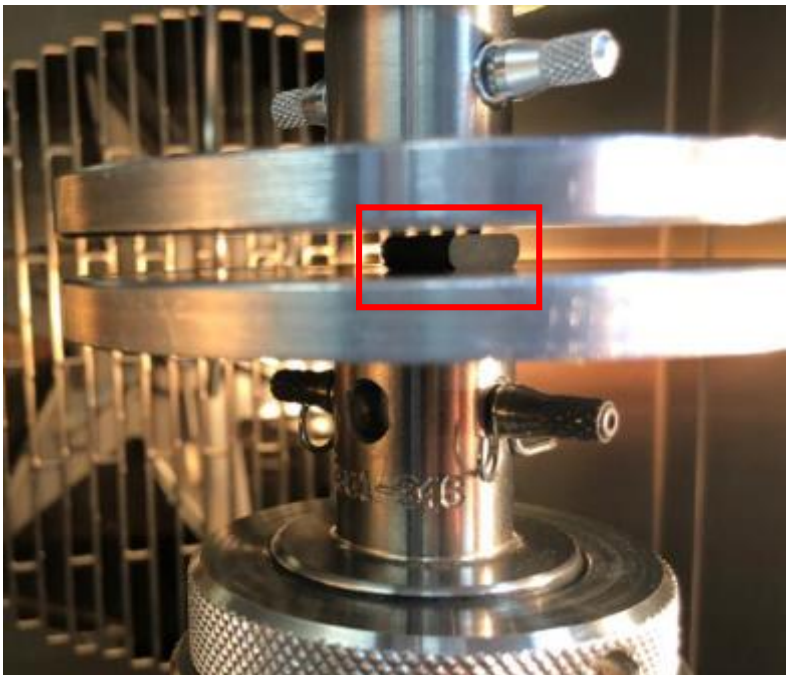

Figure C.3 A sample specimen, located between the compression plates in the red square, inside the temperature controlled chamber of the Instron 5866 machine.

Figure C.4 The Instrion 5866 electromechanical testing machine, mounted with a temperature controlled chamber.

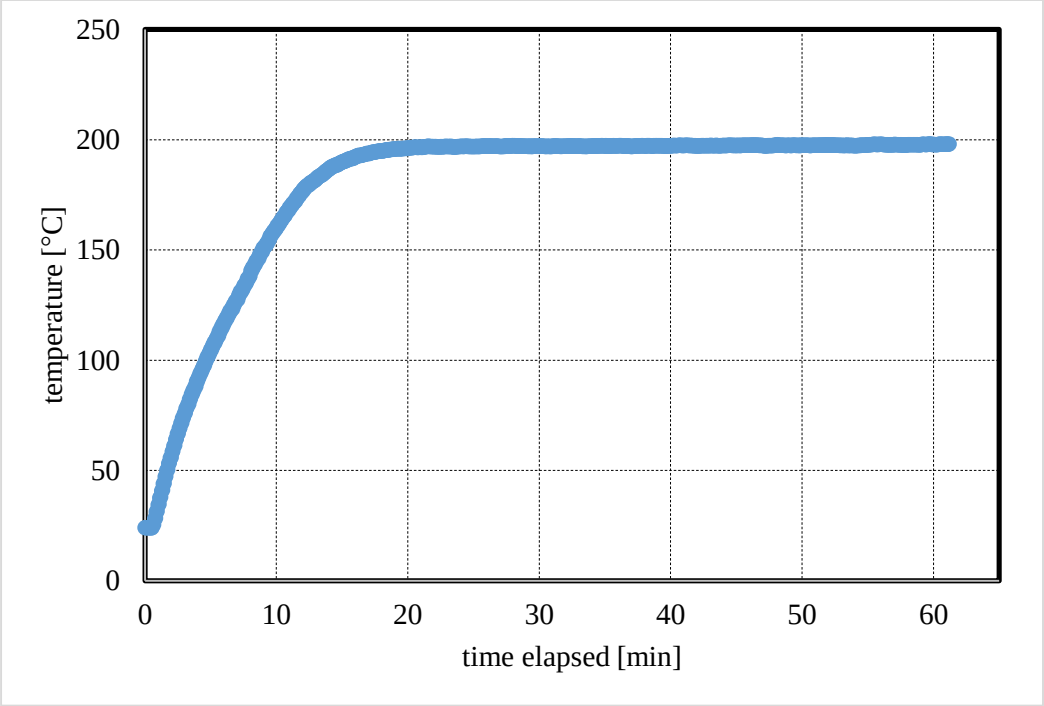

Figure C.5 The thermocouple readings as the sample was heated to a temperature of 200 °C prior to compression testing.

.

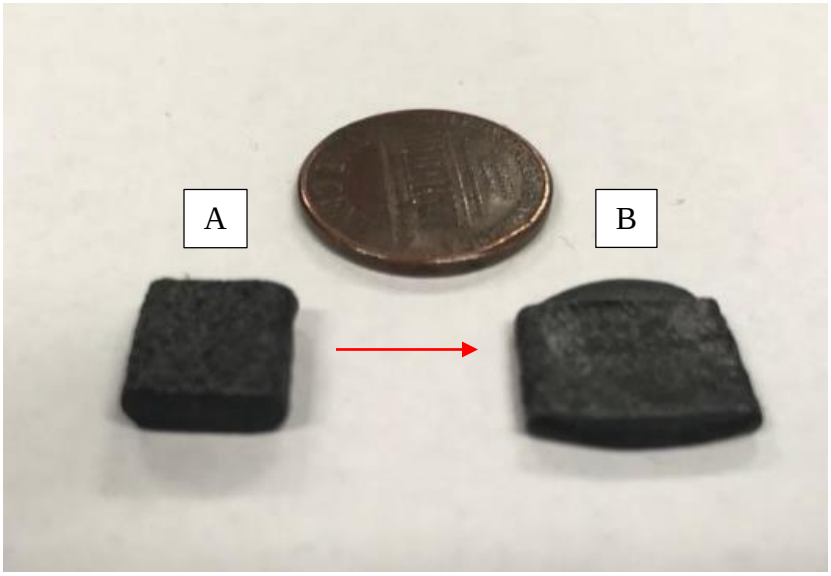

Figure C.6 Sample test coupons. Specimen A is an uncompressed sample, and specimen B is a sample after compression at 170 °C.

Figure C.7 The ATM Brilliant 220 Precision cutter, used for preparing the compression testing specimens.

Figure C.8 The ATM Saphire 530 grinder and polisher machine used to prepare the compression testing specimens.

Figure C.9 The Keyence VHX-1000 digital microscope used for the optical imaging in the porosity analysis.

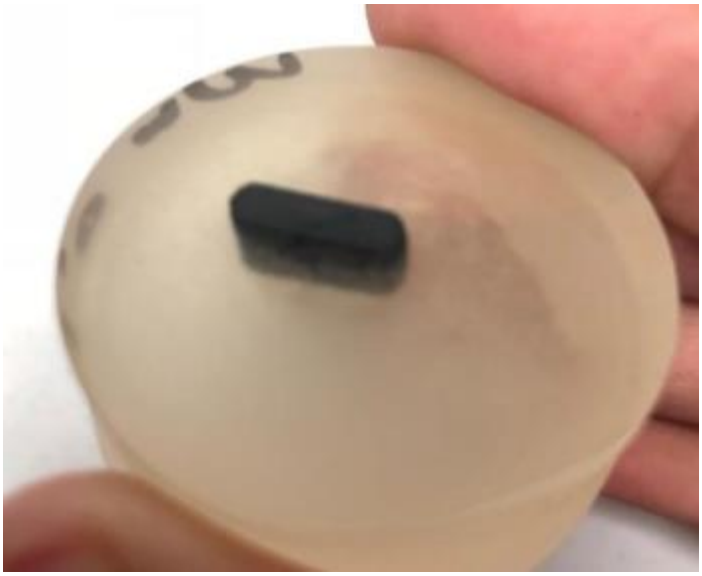

Figure C.10 A specimen mounted in resin, used in the optical imaging experiment to analyze for porosity.

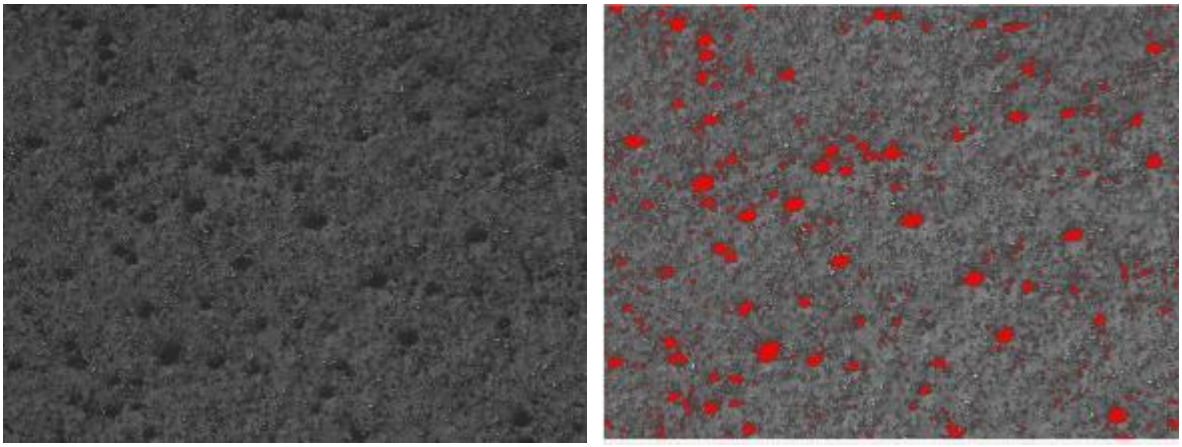

Figure C.11 The optical imaging performed on the specimen compressed at 0.2 mm. The original image is in the left and the processed image is in the right. The red areas in the right image represent the pores.

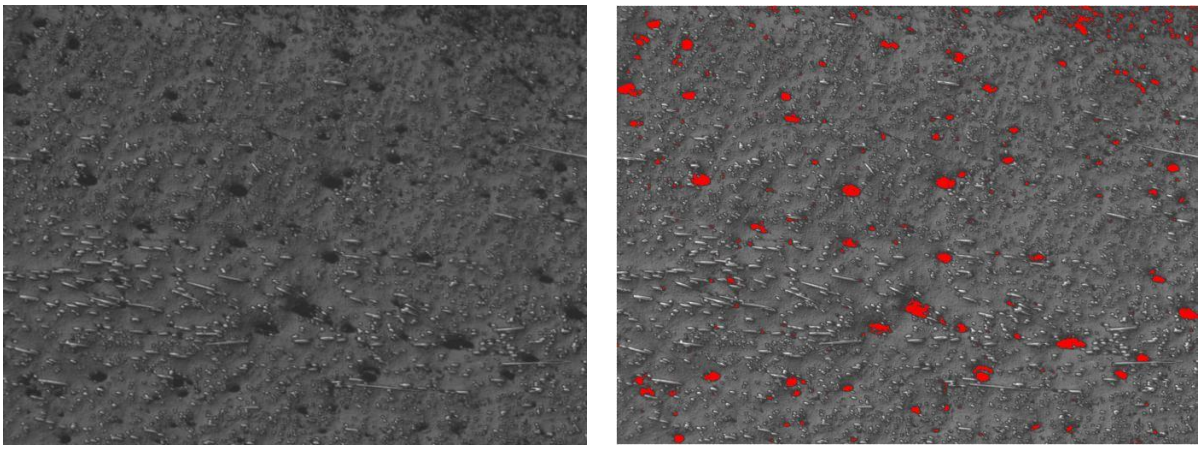

Figure C.12 The optical imaging performed on the specimen compressed at 1.0 mm. The original image is in the left and the processed image is in the right. The red areas in the right image represent the pores.

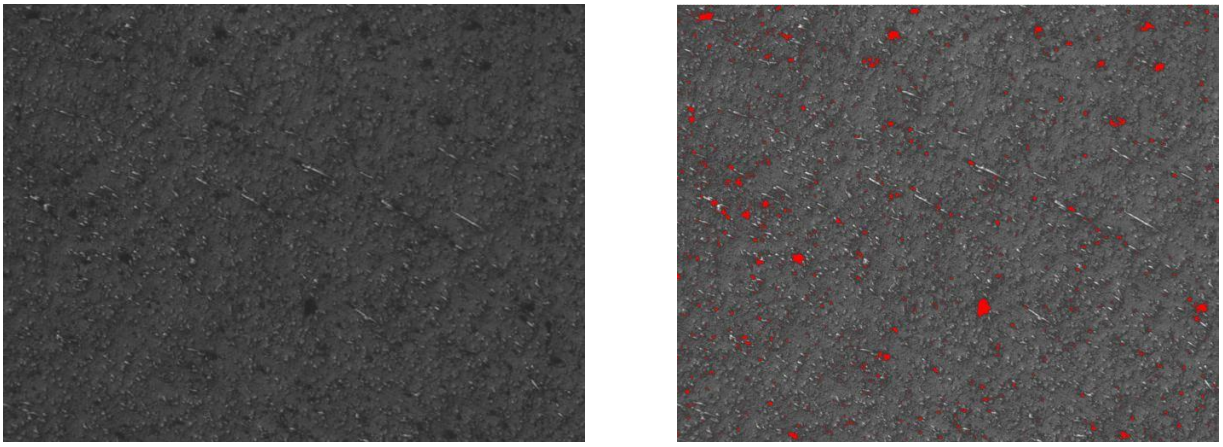

Figure C.13 The optical imaging performed on the specimen compressed at 1.2 mm. The original image is in the left and the processed image is in the right. The red areas in the right image represent the pores and fibers. A size threshold was applied to distinguish the pores and the fibers.

Figure C.14 The DHR-2 rheometer, mounted with the 25mm diameter parallel plates (inside the red square) used for the dynamic melt rheology testing experiments.

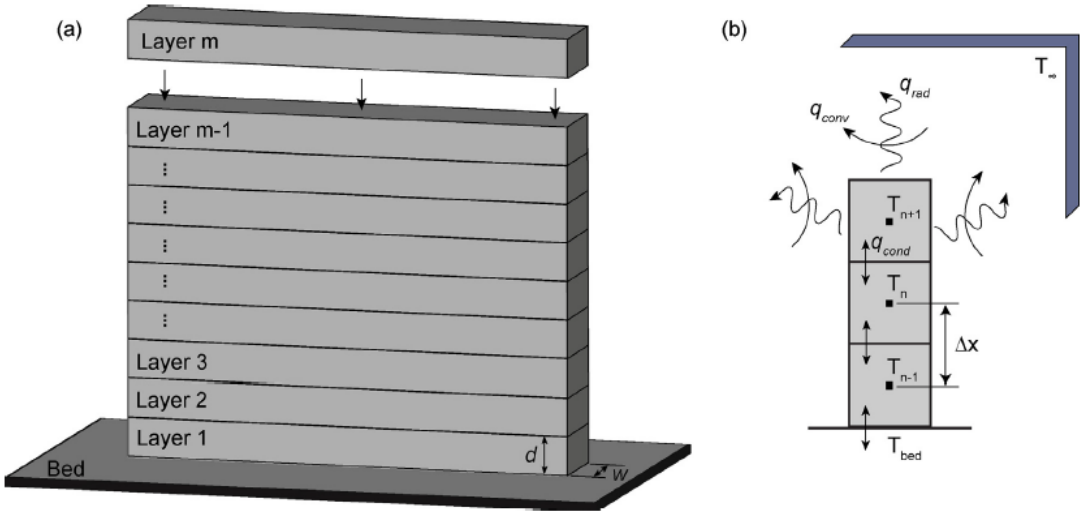

Figure C.15 The 1D thermal model schematic showing geometry (a) and boundary conditions (b) [2].

The 1D thermal model developed by Compton *et al.* [23]:

Energy balance for a control volume about the current node, where $\dot{E}_{in}$ is the rate of energy coming into the control volume, $\dot{E}_g$ is the rate of energy generation within the volume, and $\dot{E}_{st}$ is the rate of change in energy stored in the volume:

$$\dot{E_{in}}+\dot{E_g} = \dot{E_{st}} \qquad (1)$$

The energy equation (Eq. 1) is then broken into separate contributions from conduction, convection and radiation:

$$q_{cond} + q_{conv} + q_{rad} = \dot{E_{st}} \qquad (2)$$

The subscripts *cond, conv*, and *rad* represent conduction, convection, and radiation respectively. Using explicit, forward difference formulation and the boundary conditions from Figure C.9 above, Equation 2 can be represented per unit length of wall as follows, for each of the possible boundary condition sets:

$$q'_{cond} = \begin{cases} \frac{2kw}{\Delta x}\left(T_b - T_n^p\right) + \frac{kw}{\Delta x}\left(T_{n+1} - T_n^p\right), bottom\ node \\ \frac{kw}{\Delta x}\left(T_{n-1} - T_n^p\right) + \frac{kw}{\Delta x}\left(T_{n+1} - T_n^p\right), middle\ nodes \\ \frac{kw}{\Delta x}\left(T_{n-1} - T_n^p\right), top\ node \end{cases} \quad (3)$$

$$q'_{conv} + q'_{rad} = \begin{cases} \Delta x(h + h_{rad})\left(T_\infty - T_n^p\right), bottom\ node \\ 2\Delta x(h + h_{rad})\left(T_\infty - T_n^p\right), middle\ nodes \\ \Delta x(h + h_{rad})\left(T_\infty - T_n^p\right) + w(h + h_{rad})\left(T_\infty - T_n^p\right), top\ node \end{cases} \quad (4)$$

$$\dot{E}'_{st} = \begin{cases} \frac{\rho c_p w}{\Delta t}\frac{\Delta x}{2}\left(T_n^{p+1} - T_n^p\right), bottom/top\ nodes \\ \frac{\rho c_p w}{\Delta t}\Delta x\left(T_n^{p+1} - T_n^p\right), middle\ nodes \end{cases} \quad (5)$$

In these equations, Δt is the time increment, Δx is the nodal spacing, n is the current node, and p is the current time increment. The material properties, h, and k, are outlined in Table 3.1, corresponding to ABS-20CF. The radiative heat transfer coefficient, h_{rad}, is given by Equation 6 below, and it is calculated for every node at every time increment:

$$h_{rad} = \varepsilon\sigma\left(T_\infty + T_n^p\right)\left(2T_n^p + T_\infty^2\right) \quad (6)$$

In Equation 6, ε is the emissivity of the material, and σ is the Steffan-Boltzman's constant of 5.67 10^{-8} W/m^{2}K^4. Substituting equations (3), (4), and (5) into (2) solves for the new temperature T_n^{p+1}, for the current node n.

The full solution iterates through all the nodes in the model for time period Δt_{layer}, after which a new set of nodes with temperature of T_{dep} is added to the model, representing a newly deposited layer. The solver again iterates through all nodes for the time period Δt_{layer}. Each new layer brings additional energy into the model. The rate of energy deposited per unit length is given as:

$$q'_{dep} = \frac{wd\rho c_p T_{dep}}{\Delta t_{layer}} \quad (7)$$

The numerical solution is stabilized by taking the minimum of the stable time step values calculated for each boundary condition using the Fourier stability criterion, where the coefficient of T_n^p in (5) is less or equal to zero, as seen in Equation 8 below:

$$q'_{cond} = \begin{cases} \left[\frac{12k}{\rho c \Delta x^2} + \frac{2\left(h + h_{rad,max}\right)}{\rho c w}\right]^{-1}, bottom\ node \\ \left[\frac{2k}{\rho c \Delta x^2} + \frac{2\left(h + h_{rad,max}\right)}{\rho c w}\right]^{-1}, middle\ nodes \\ \left[\frac{2k}{\rho c \Delta x^2} + \frac{2\left(h + h_{rad,max}\right)}{\rho c w} + \frac{2\left(h + h_{rad,max}\right)}{\rho c \Delta x}\right]^{-1}, top\ node \end{cases} \quad (8)$$

Finally, to ensure the most conservative time step, the maximum possible value is used for the radiation heat transfer coefficient, given by Equation 9 below:

$$h_{rad,max} = \varepsilon\sigma\left(T_\infty + T_{dep}\right)\left(T_{dep}^2 + T_\infty^2\right) \quad (9)$$

The MATLAB code developed at the W.M. Keck Center for 3D Innovation to implement the 1D thermal model in Compton *et al.*:

```
% 1-D Heat Transfer modified Model for BAAM
% Based on work by ORNL-MDF, Compton
% The model looks at the temp of the top layer to see if it's above
the
% tresshold, if not, it adds additonal time to the layer time
% Copyright Xavier Jimenez 2018
clc
clear all
% Define Material Properties
global k c_p T_g p e h delta T_dep T_bed T_amb d L w dx time T ii j T1
layers
k = 0.17; % Thermal Conductivity [W/m*K]
c_p = 1640; % Specific heat capacity [J/Kg*K]
T_g = 110; % Glass transition temperature [degrees C]
p = 1140; % Density [Kg/m^3]
e = 0.87; % Emissivity
h = 8.5; % Natural convection coefficient [W/m^2*K]
delta = 0.0000000567; % Boltzman's constant
% Define printing parameters
T_dep = 238; % Deposition temperature [degrees C]
T_bed = 65; % Bed temperature [degrees C]
T_amb = 18; % Ambient temperature [degrees C]
d = 4.064; % Layer height [mm]
L = 0.358; % Wall height [m]
w = 0.02; % Wall thickness [m]
dx = 0.00254; % Nodal spacing [m]
layers = 18;
time = 50;
T = zeros (layers,1000,layers); % preallocation for speed
ii = 0;
for j = 1:1:layers
T(j,1,j) = T_dep; %New layer at T_dep is added every iteration
jj = 0;
for dt = 1:1:time % time steps from 1 to 10 layers time, with a layer
time of time [s]
ii = 1 + ii;
jj = jj + 1;
for i = 1:1:j
h_rad = e*delta*(T(i,dt,j) + T_amb)*(T(i,dt,j)^2 + T_amb^2);
if i == 1
%bottom node
T(i,dt+1,j) = ((((2*k*w)/dx)*(T_bed - T(i,dt,j)) + ((2*k*w)/
dx)*(T(i+1,dt,j) - T(i,dt,j)) + dx*(h + h_rad)*(T_amb - T(i,dt,j))))/

((p*c_p*w*dx)/(2*0.77))) + T(i,dt,j);



elseif i == j
```

```
%top formula
T(i,dt+1,j) = ((((k*w)/dx)*(T(i-1,dt,j) - T(i,dt,j)) + (dx*(h
+ h_rad)*(T_amb - T(i,dt,j))) + w*(h + h_rad)*(T_amb - T(i,dt,j)))/
((p*c_p*w*dx)/(2*0.77))) + T(i,dt,j);
else
%middle formula
T(i,dt+1,j) = ((((k*w)/dx)*(T(i-1,dt,j) - T(i,dt,j)) +
((k*w)/dx)*(T(i+1,dt,j) - T(i,dt,j)) + 2*dx*(h + h_rad)*(T_amb -
T(i,dt,j)))/((p*c_p*w*dx)/(0.77))) + T(i,dt,j);
end
for ww = 1:layers % This for loop is use to transfer the T values
from 3D array to 2D array
T1(ww,ii) = T(ww,jj,j);
end
T(:,1,j+1) = T(:,time,j); % transfer the values of the last time step
towards the next layer time step 1
end
end
if T1(j,ii) > 200 % Checking temperature of top most layer
Temp
end
layer_time(j) = time;
end
szdim2 = size(T1,2);
t = 1:1:szdim2; %Plot of the 2D aaray
plot(t,T1);
xlabel('Time (s)')
ylabel('Temperature C')

%hold on
```

Appendix D

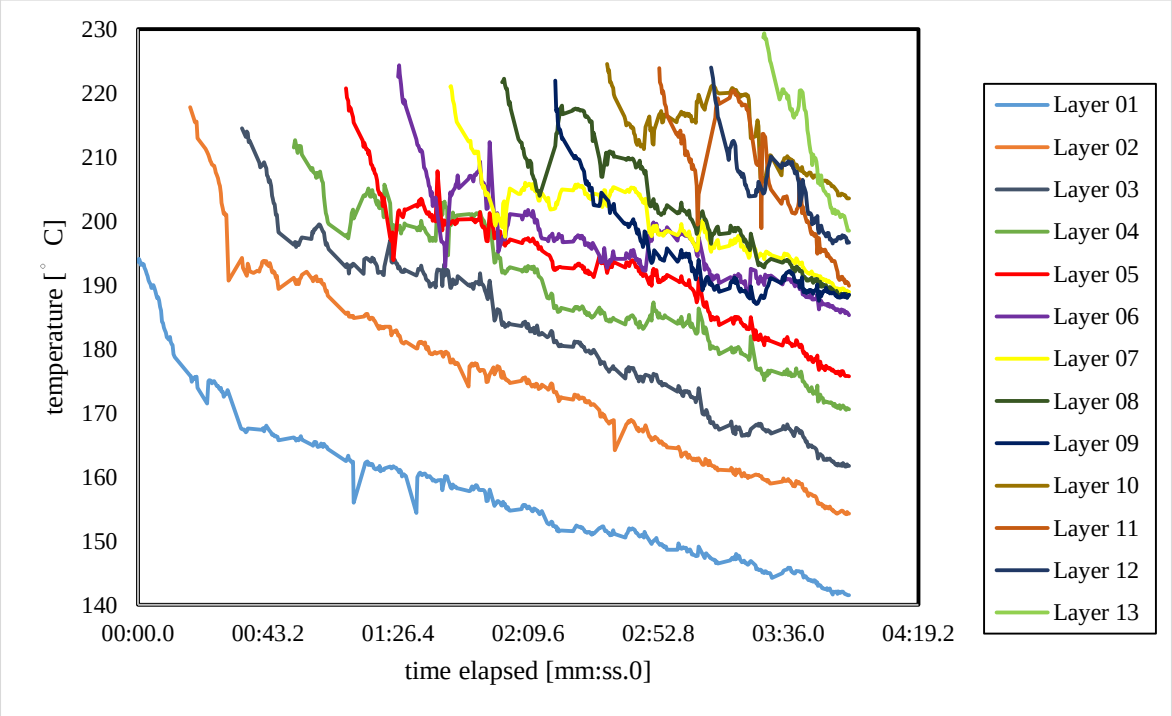

Figure D.1 The thermography of the hexagon geometry printed with no added layer time. In the final layers, the layer deformation interfered with the analysis points, hence the behavior of layer 11.

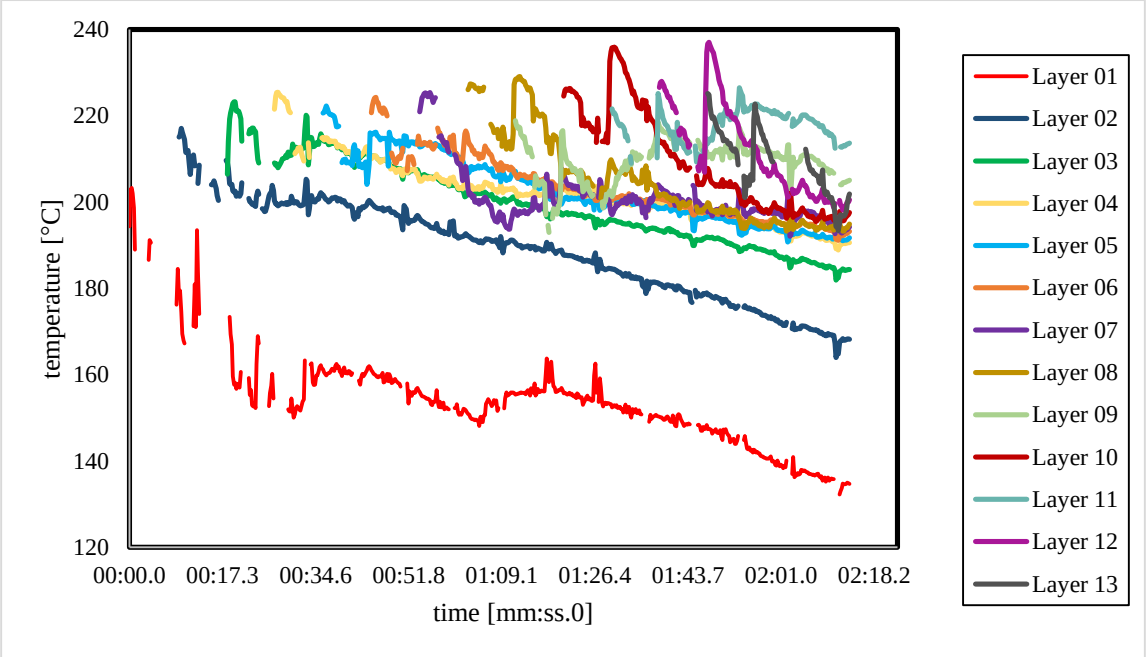

Figure D.2 The thermal history of every layer printed in the single-bead thin wall geometry. Deformation in the print interfered with the thermography analysis points.

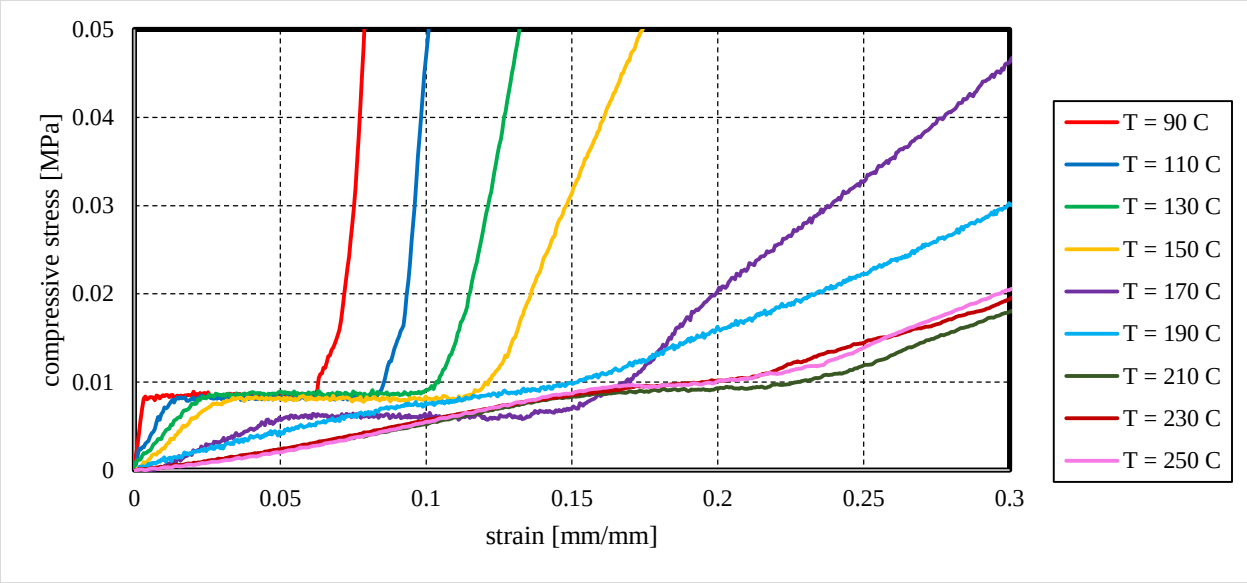

Figure D.3 The average compression behavior for every one of the nine temperature sets. The plateau region at low strain levels is attributed to the initial joggle of the compression plates.

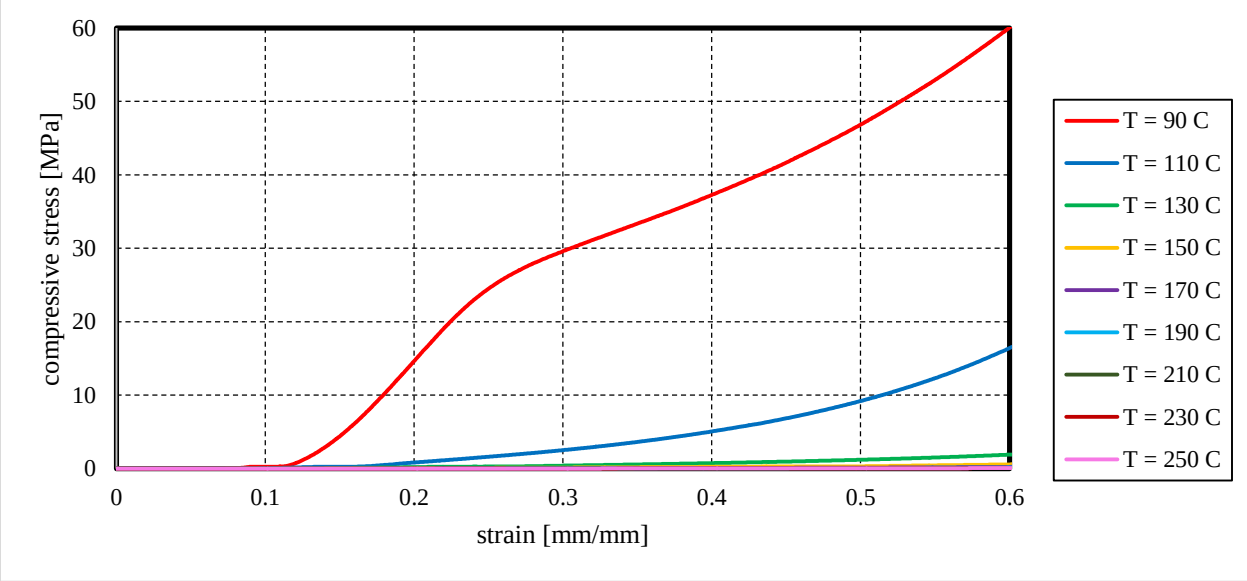

Figure D.4 The average compression behavior for every one of the nine temperature sets, showing the entire range of strain and loading present during testing. Notice the significant difference between the compression behavior at 90 °C and 110 °C. This highly noticeable change is due to the temperature rising above the T_g for ABS-20CF.

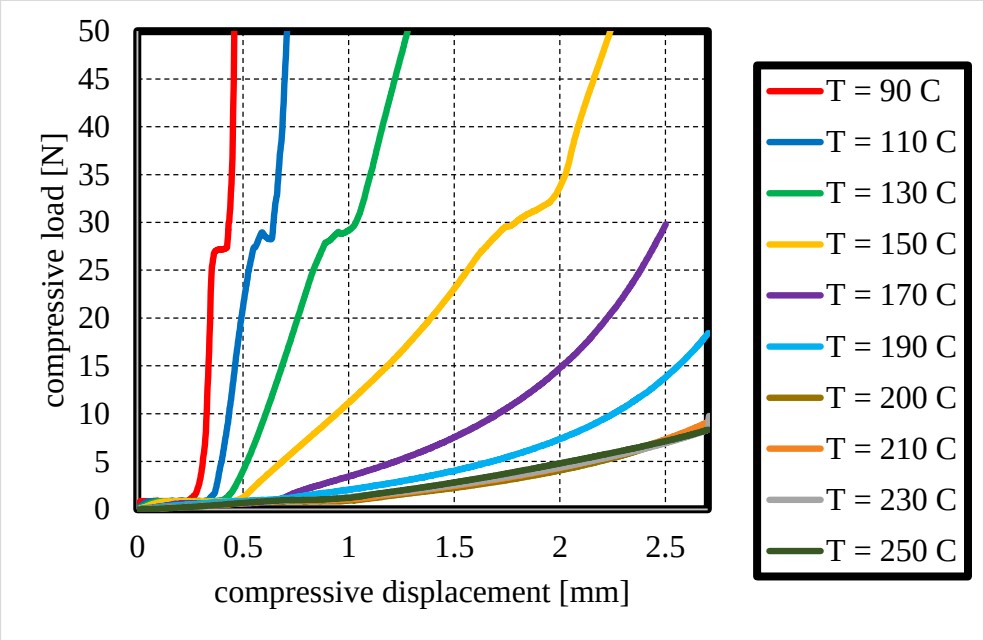

Figure D.5 The average compression behavior for every one of the nine temperature sets. The plateau region at low strain levels is attributed to the initial joggle of the compression plates.

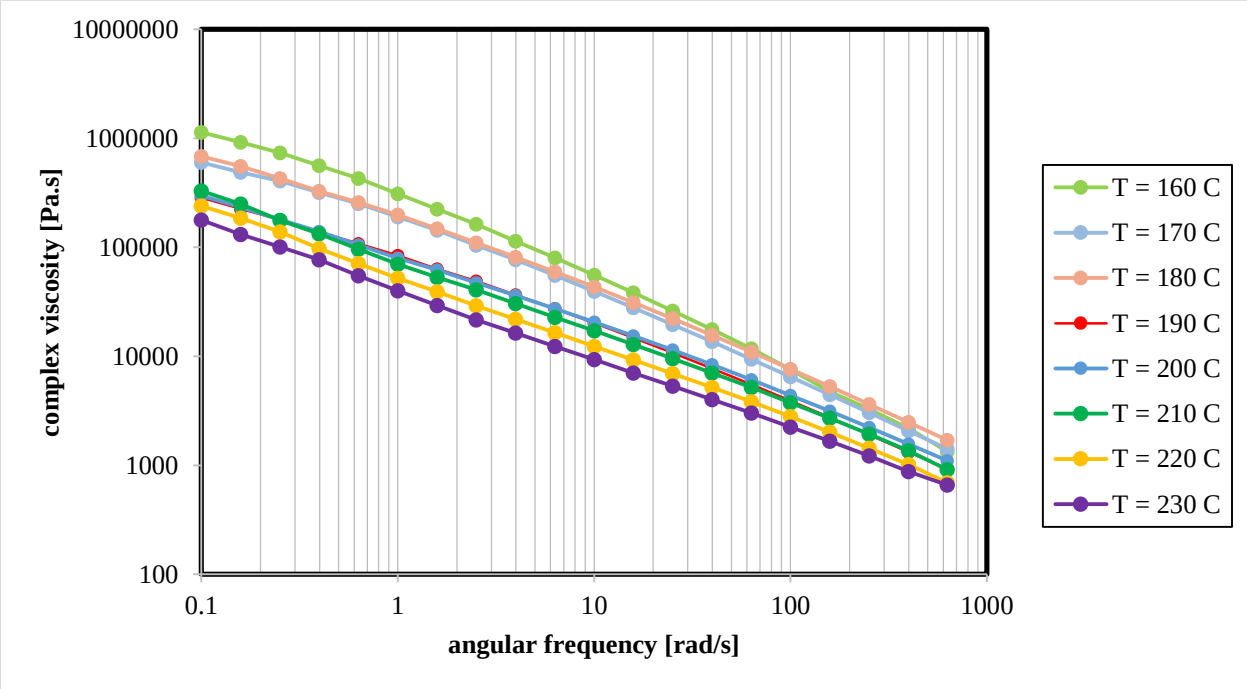

Figure D.6 The complex viscosity of ABS-20CF. Notice the inverse relationship between the complex viscosity and temperature.

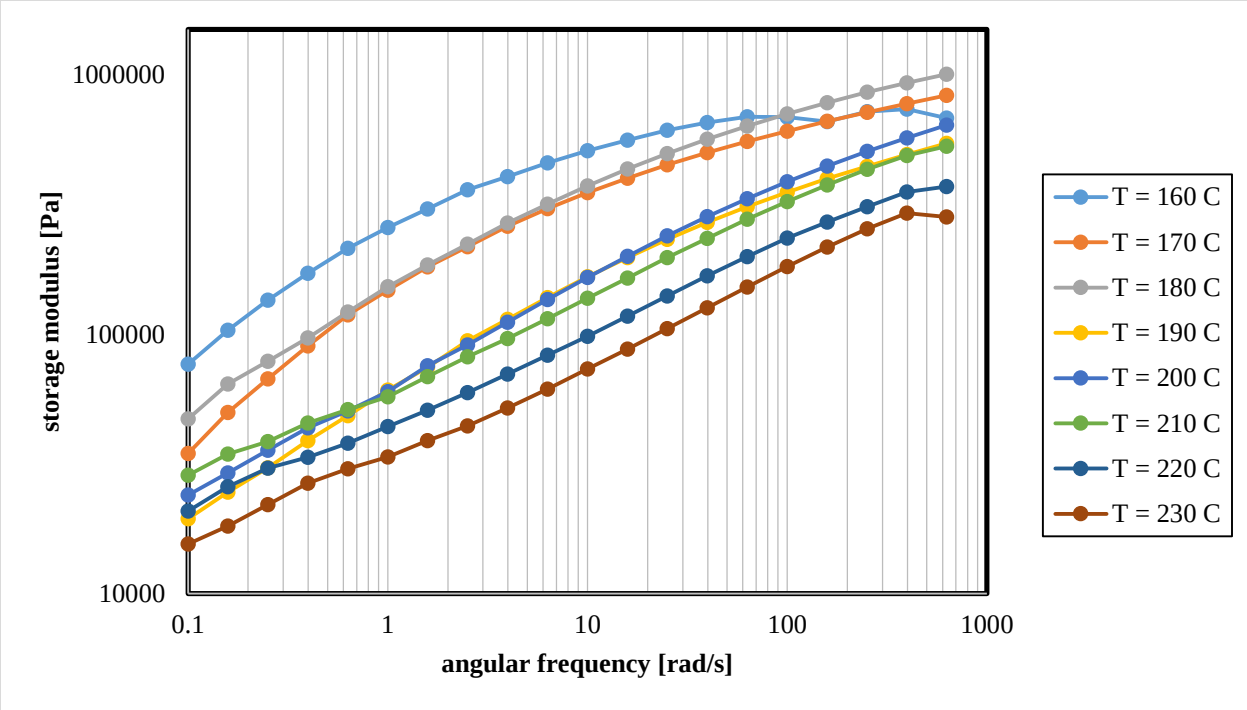

Figure D.7 The storage modulus of ABS-20CF.

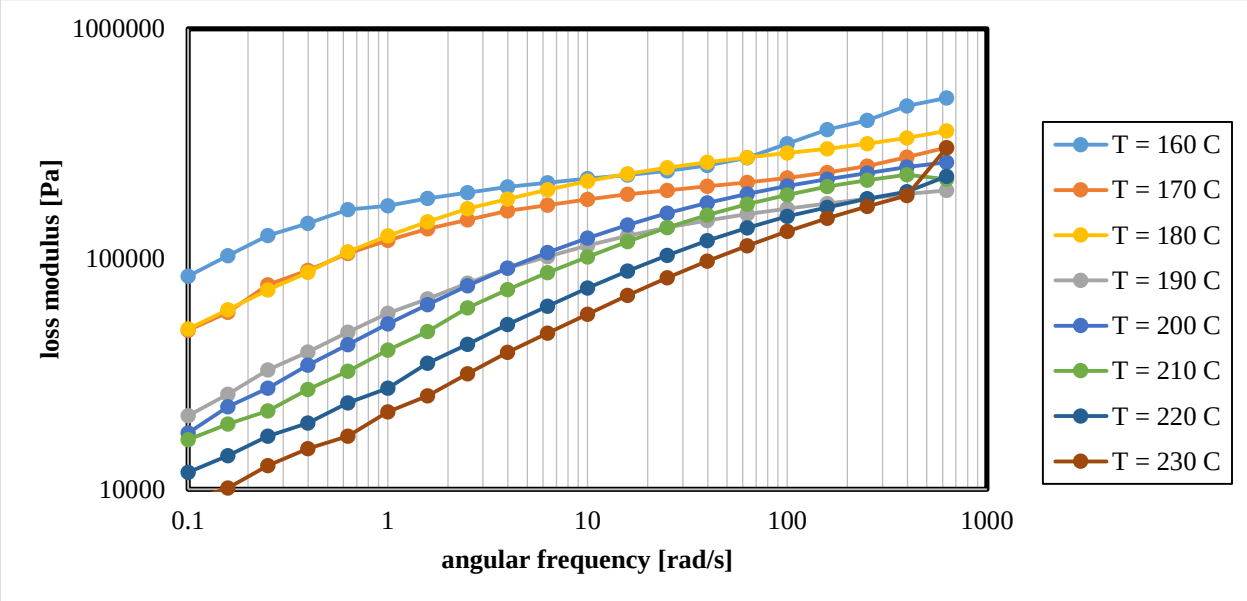

Figure D.8 The loss modulus of ABS-20CF.

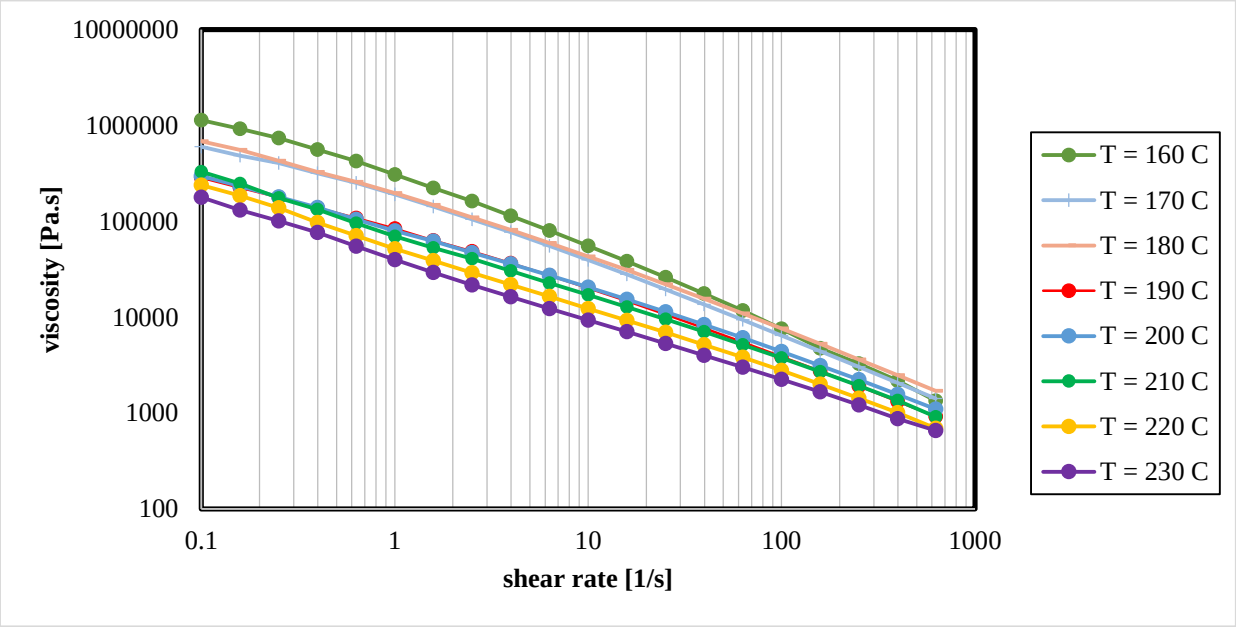

Figure D.9 The Cox-Merz transformation of the rheological analysis, illustrating the viscosity of ABS-20CF as a function of shear rate.

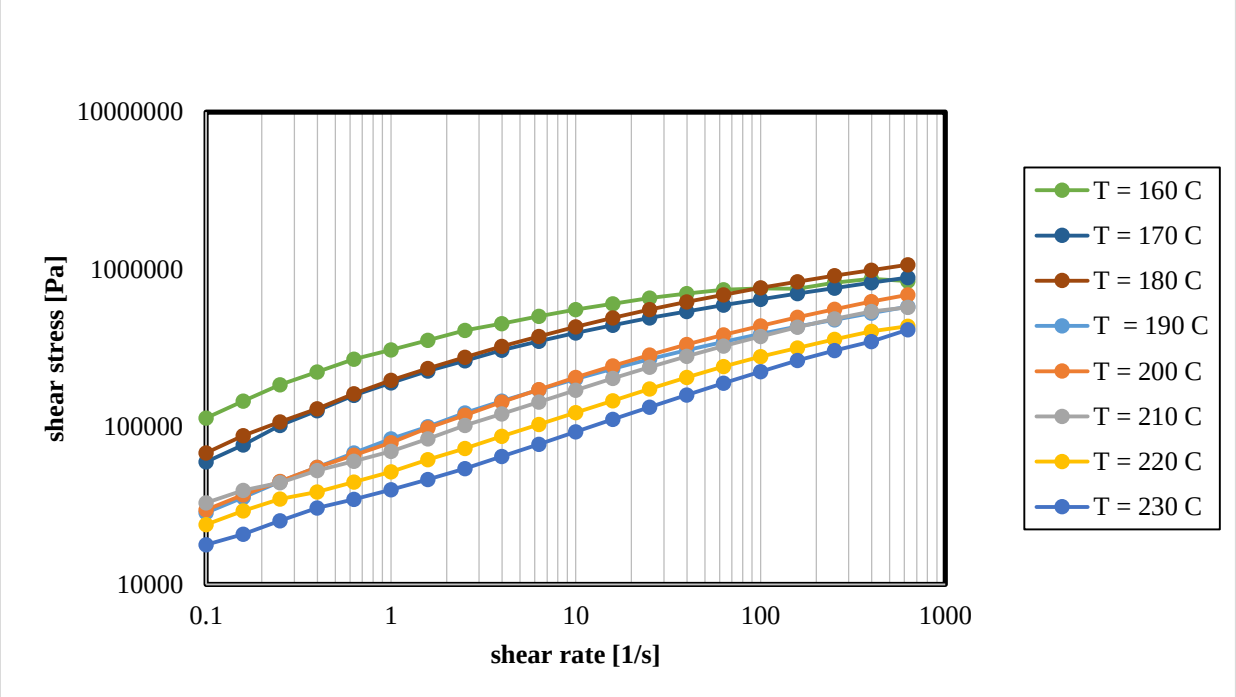

Figure D.10 The Cox-Merz transformation of the rheological analysis, illustrating the shear stress of ABS-20CF as a function of shear rate.

Vita

Eduardo Meraz Trejo was born in the state of Chihuahua, Mexico. He obtained a high school diploma from Cathedral High School, located in El Paso, Texas, in 2011. He then obtained a Bachelor of Science in Mechanical Engineering and a Bachelor of Arts in Economics degree from the University of Notre Dame in 2015 and 2016 respectively. After graduation, Eduardo worked in the greater Los Angeles area for a year in a small aerospace manufacturing company. After that, he decided to attend the University of Texas at El Paso to pursue his Master of Science Degree in Mechanical Engineering. While pursuing a graduate degree, Eduardo worked as a teaching assistant in the Department of Mechanical Engineering and as a graduate research assistant in the W.M. Keck Center for 3D Innovation at the University of Texas at El Paso. Following the completion of his Master of Science in Mechanical Engineering degree, Eduardo will take on the role as Materials and Process Engineer at the Skunk Works, the Advanced Development Programs division of the Lockheed Martin Corporation.

Contact Information: emeraztrej@miners.utep.edu

This thesis was typed by Eduardo Meraz Trejo.